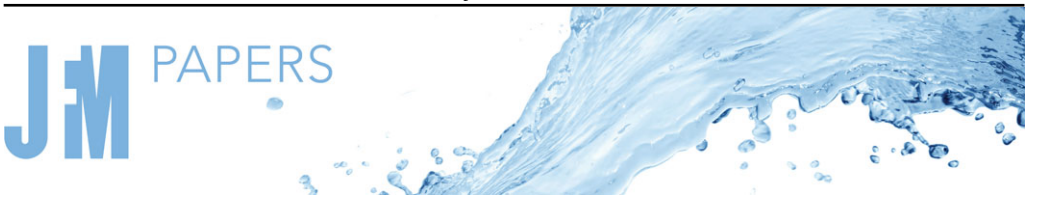
J. Fluid Mech. (2025), *vol.* 1010, A18, doi:10.1017/jfm.2025.332



Aerodynamic performance of a transonic airfoil with spanwise forcing

Niccolò Berizzi[1], **Davide Gatti**[2], **Giulio Soldati**[3], **Sergio Pirozzoli**[3] and **Maurizio Quadrio**[1]

[1]Dipartimento di Scienze e Tecnologie Aerospaziali, Politecnico di Milano, Via La Masa 34, Milano 20156, Italy

[2]Institute of Fluid Mechanics, Karlsruhe Institute of Technology, Kaiserstraße 10, Karlsruhe 76131, Germany

[3]Dipartimento di Meccanica e Aeronautica, Università di Roma 'La Sapienza', Via Eudossiana 18, Roma 00184, Italy

Corresponding author: Maurizio Quadrio, maurizio.quadrio@polimi.it

(Received 19 October 2024; revised 3 February 2025; accepted 18 March 2025)

Spanwise wall forcing in the form of streamwise-travelling waves is applied to the suction side of a transonic airfoil with a shock wave to reduce aerodynamic drag. The study, conducted using direct numerical simulations, extends earlier findings by Quadrio *et al.* (*J. Fluid Mech.* vol. 942(R2), 2022, pp. 1–10) and confirms that the wall manipulation shifts the shock wave on the suction side towards the trailing edge of the profile, thereby enhancing its aerodynamic efficiency. A parametric study over the parameters of wall forcing is carried out for the Mach number set at 0.7 and the Reynolds number at 300 000. Similarities and differences with the incompressible plane case are discussed; for the first time, we describe how the interaction between the shock wave and the boundary layer is influenced by flow control via spanwise forcing. With suitable combinations of control parameters, the shock is delayed, which results in a separated region whose length correlates well with friction reduction. The analysis of the transient process following the sudden application of control is used to link flow separation with the intensification of the shock wave.

Key words: compressible turbulence, turbulence control

1. Introduction

Environmental pollution and global warming driven by CO_2 emissions are severe global concerns; the civil aeronautical sector is a significant contributor. The United Nations' International Civil Aviation Organization (ICAO) forecasts a triplication of the aviation

© The Author(s), 2025. Published by Cambridge University Press.

https://doi.org/10.1017/jfm.2025.332 Published online by Cambridge University Press

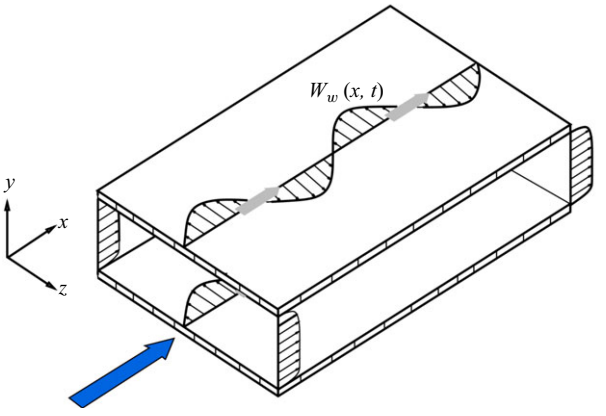


Figure 1. Sketch of wall manipulation through streamwise-travelling waves of spanwise velocity in a channel flow set-up. Figure adapted from Gatti & Quadrio (2016).

emissions by 2050, accounting for 25 % of the global carbon budget (Graver, Zhang & Rutherford 2019). Hence, the quest to reduce atmospheric pollutants, alongside pressing economic reasons, motivates the industry efforts towards more efficient vehicles. In air transportation, the roughly linear dependency of fuel consumption on aerodynamic resistance drives research into flow control methods for drag reduction. However, controlling turbulence in flow conditions typical of transport applications presents many scientific and engineering challenges. In mature applications involving fluid flows, drag – particularly skin-friction drag, which is intimately related to the turbulent nature of high-Reynolds-number flows – is difficult to abate.

Flow control techniques aimed at friction reduction are usually classified into passive and active. The latter require extra energy but can yield higher net energetic benefits. Among them, spanwise forcing based on a space- and/or time-dependent distribution of spanwise velocity at the wall stands out for its energy-saving potential. Several implementations of spanwise forcing were considered over the years, starting from the simplest spanwise-oscillating wall, introduced by Jung, Mangiavacchi & Akhavan (1992) and thoroughly studied by Quadrio & Ricco (2004), in which the spanwise motion of the wall is uniform in space and varies harmonically in time. The most promising technique of this class is the combined space–time version, i.e. the streamwise-travelling waves of spanwise velocity (hereinafter, StTWs), introduced years later by Quadrio, Ricco & Viotti (2009). This technique involves manipulating the wall velocity W_w according to

$$W_w(x, t) = A \sin(\kappa_x x - \omega t), \tag{1.1}$$

where x and t are the streamwise coordinate and time, respectively, while A, κ_x and ω are the control amplitude, and the spatial and temporal frequencies of the forcing, respectively (see figure 1 for a sketch). Quadrio & Ricco (2011) qualitatively explained the working mechanism of the StTWs: the waves generate a transversal Stokes layer (whose thickness is determined by the control parameters), which interacts favourably with the near-wall turbulence. The effectiveness of StTWs has received experimental verification: Auteri *et al.* (2010) measured up to 33 % drag reduction in a pipe flow by spatially discretising the sinusoidal waveform with independently rotating pipe slices; Bird, Santer & Morrison (2018) developed a planar actuator for StTWs, consisting of a tensioned membrane skin mounted on a kagome lattice; Marusic *et al.* (2021) and Knoop *et al.* (2024) extended the spatially discrete actuator of Auteri *et al.* (2010) to the planar geometry. Finally, the recent

https://doi.org/10.1017/jfm.2025.332 Published online by Cambridge University Press

contribution by Gallorini & Quadrio (2024) has led to a satisfactory understanding of the discrete form of the forcing.

These promising results mostly derive from studies of incompressible flows in simple planar geometries and at relatively low Reynolds numbers (Re). While the Re-dependence has been thoroughly discussed by Gatti & Quadrio (2016), flow compressibility has been put into focus more recently. Yao & Hussain (2019) found that compressibility leads to additional drag reduction in a supersonic channel with oscillating walls. However, Gattere *et al.* (2024), in addition to considering the general StTW case, reviewed the procedure to compare controlled and uncontrolled cases, and concluded that the power budget of StTWs in planar geometry is essentially unaffected by flow compressibility, once the comparison is properly conducted. Nevertheless, StTWs have rarely been analysed in the compressible regime in combination with non-planar walls, despite this being the typical application scenario in aeronautics, where shock waves can develop, and pressure and friction contributions are comparable in the global drag budget (Abbas, de Vicente & Valero 2013).

The idea that control techniques for friction drag reduction might affect pressure drag was put forward by Mele, Tognaccini & Catalano (2016), who performed Reynolds-averaged Navier–Stokes (RANS) simulations around a transonic wing-body configuration with riblets installed. Banchetti, Luchini & Quadrio (2020) verified via direct numerical simulation (DNS) that this is indeed the case for StTWs in an incompressible flow over a non-planar wall. Finally, Quadrio *et al.* (2022) applied StTWs in a physically richer scenario, relaxing both the planarity and incompressibility assumptions. They employed DNS to describe the turbulent flow over a modern transonic aerofoil where a shock wave develops. StTWs were applied to a portion of the suction side of the wing, and their effects were measured in terms of global lift and drag forces, together with the evolution of friction and pressure along the chord. They observed that StTWs affect both friction and pressure distributions, with the most significant flow modifications ensuing from changes in the position and intensity of the shock wave. Specifically, a more intense and delayed shock was observed, leading to a significant improvement in the aerodynamic efficiency of the wing. At the lower incidence that re-establishes the required lift with the control enabled, a net reduction of 9 % was estimated for the drag of the entire aircraft.

In this work, we extend these results and seek a deeper physical understanding. We keep using StTW forcing that is interesting because of its large local drag reduction and net savings, which make the global effects more self-evident; its hassle-free implementation in a simulation via boundary conditions is attractive. The original study of Quadrio *et al.* (2022) only tested two StTW configurations, where the control parameters were selected based on the incompressible information; the extent and position of the active surface area were deduced empirically. Moreover, a characterisation of the physics behind the control-induced flow changes was not attempted. In this study, we intend neither to carry out a full optimisation of StTWs for this particular aerofoil nor to assess the effects of compressibility alone, for which the picture described by Gattere *et al.* (2024) is exhaustive enough for the planar geometry. Instead, we set two goals. The first is to explore the parameter space defined by the control variables (A, κ_x, ω), and augmented by the position and extent of the actuated region to identify analogies and differences with the plane channel flow. The second is to describe how the control alters the complex physics of the flow, characterised by the mutual interaction of the shock wave and the turbulent boundary layer.

The paper is structured as follows: in § 2, we describe the flow configuration and the numerical tools adopted in the analysis; in § 3, the aerodynamic performance of the system subject to spanwise forcing is studied; in § 4, we address the flow physics, focusing first on

https://doi.org/10.1017/jfm.2025.332 Published online by Cambridge University Press

the evolution of the boundary layer along the chord in § 4.1 and then on the response of the flow after the sudden imposition of the forcing in § 4.2; finally, a concluding discussion is presented in § 5.

2. Numerical methods and procedures

2.1. *DNS solver and computational set-up*

The DNS solver used in this study is the same as that employed by Quadrio *et al.* (2022), and was extensively described and validated earlier by Memmolo, Bernardini & Pirozzoli (2018). The compressible Navier–Stokes equations are solved for an ideal gas, with the heat flux vector and the viscous stress tensor modelled by Fourier's law and the Newtonian hypothesis, respectively. The dependence of dynamic viscosity μ on temperature T is described by the power law $\mu/\mu_\infty = (T/T_\infty)^{0.76}$ (Smits & Dussauge 2006). Here and throughout the paper, the subscript '∞' refers to the free stream undisturbed flow. The equations, cast in integral form, are discretised using a second-order, energy-consistent finite-volumes method (Pirozzoli 2011). In the presence of shock waves, detected by a modified Ducros sensor (Ducros *et al.* 1999), the code switches locally to a third-order weighted essentially non-oscillatory scheme (Liu, Osher & Chan 1994).

The case of interest is the same as that considered by Quadrio *et al.* (2022), i.e. an aerofoil immersed in a uniform flow. The sectional profile is the supercritical V2C aerofoil, designed within the European project TFAST (Doerffer *et al.* 2021), and already studied experimentally (Placek & Ruchala 2018) and numerically (Szubert *et al.* 2016; Zauner, De Tullio & Sandham 2019). The angle of attack is $\alpha = 4°$, which provides the maximum lift-to-drag ratio. The airflow has inflow conditions of Mach number $M_\infty \equiv U_\infty/a_\infty = 0.7$ (where U_∞ is the free stream velocity and a_∞ is the speed of sound in the free stream) and Reynolds number $Re_\infty \equiv U_\infty c/\nu_\infty = 3 \times 10^5$ (where c is the profile chord and ν_∞ is the kinematic viscosity in the free stream). Periodicity is enforced in the spanwise direction and the inflow is laminar: to avoid the large excursions of the transition location (Zauner *et al.* 2019), the boundary layer is tripped, as in experiments. A small Gaussian blob of wall-normal random volume force (Schlatter & Örlü 2012) acts on both sides of the aerofoil $0.1c$ downstream of the leading edge. The intensity of the tripping force ($100U_\infty^2/c$) was selected as the minimum value granting healthy development of the turbulent boundary layer.

Unless otherwise indicated, the length scale c and velocity scale U_∞ are used to form dimensionless quantities, and are omitted hereinafter. Alternatively, viscous units will also be adopted, where the reference velocity is the friction velocity ($u_\tau = \sqrt{\tau_w/\rho}$) and the reference length is the viscous length (ν/u_τ). In these definitions, τ_w, ρ, ν are the wall-shear stress, density and kinematic viscosity, respectively. Quantities made non-dimensional with the viscous units extracted from the reference uncontrolled simulation are denoted with a '$+$' superscript, while the '$*$' scaling denotes quantites made non-dimensional with the friction velocity of the current simulation. Note, however, that the wall-shear stress varies significantly along the profile. In this paper, friction is evaluated on the suction side at $x = 0.4$, a position that is downstream enough for the actuation to actually develop its effects, but also sufficiently upstream of the shock such that the wall pressure gradient is almost constant across the various simulations. This aspect is further discussed in § 3.2 and in Appendix A.

The computational set-up replicates the baseline case described by Quadrio *et al.* (2022), who validated it in terms of resolution requirements. The mesh features a C-type topology with $4096 \times 512 \times 256$ cells. It has a radius 25 chords and a spanwise extension of

https://doi.org/10.1017/jfm.2025.332 Published online by Cambridge University Press

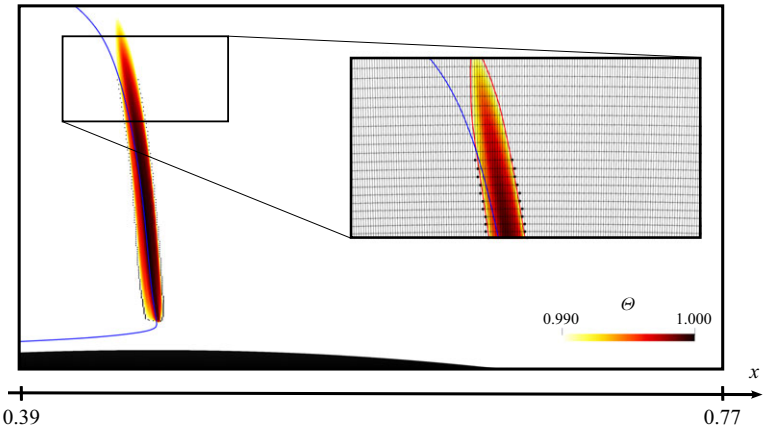


Figure 2. Visualisation of the mean modified Ducros shock sensor over the suction side of the aerofoil (reference simulation), highlighting regions where $\Theta > 0.99$. The blue line is the isoline at $M = 1$ and the black dots denote the cells used to compute the shock intensity. The inset shows the upper edge of the shock superimposed to the grid, with the red isoline corresponding to $\Theta = 0.99$.

$L_z = 0.1$, which is sufficiently large to grant that the flow statistics are independent from this length. For verification, an additional simulation was carried out for the reference flow with a spanwise extension of $L_z = 0.4$, only to find overlapping results. The cells are uniformly spaced in the spanwise direction, while a hyperbolic-tangent clustering is adopted in the wall-normal direction. The mesh meets the requirements for a fully resolved DNS, with $\Delta x^+ < 10$, $\Delta y^+ < 0.5$ and $\Delta z^+ < 5$ at the wall, where Δx, Δy and Δz are the grid spacings in the x, y and z directions, respectively. Curvilinear coordinates ξ and η will be used in the following to denote directions tangent and normal to the wall, respectively. Time integration is performed using a low-storage, third-order Runge–Kutta scheme, with a fixed time step of $\Delta t = 1.2 \times 10^{-4}$, chosen to keep the maximum Courant–Friedrichs–Lewy number below unity. The quantities of interest are averaged in the spanwise direction and over time for a minimum duration of $\Delta T = 40$; the most significant cases, discussed in the next section, are run for a maximum $\Delta T = 130$. The initial transient, determined on a case-by-case basis, is excluded from the time-averaging process. An *a posteriori* analysis of the lift and drag time histories using the algorithm developed by Russo & Luchini (2017) confirms that the ratio between the standard deviation σ of the estimated mean value of the lift coefficient and the coefficient's value remains below 0.4 % across all cases; the same quantity for the drag coefficient is below 0.7 %. These metrics are presented as σ_L and σ_D in table 1.

The discussion that follows will consider the position and strength of the shock wave. To identify the shock, we use the modified Ducros sensor (Pirozzoli 2011)

$$\Theta = \max\left(-\frac{\boldsymbol{\nabla}\cdot\boldsymbol{u}}{\sqrt{(\boldsymbol{\nabla}\cdot\boldsymbol{u})^2 + (\boldsymbol{\nabla}\times\boldsymbol{u})^2 + (U_\infty/c)^2}}; 0\right) \tag{2.1}$$

where $\boldsymbol{u}$ is the local velocity vector. Figure 2 displays the mean value of Θ near the shock wave for the reference case. We define a point to be within the shock if $\Theta > 0.99$. The shock position, denoted with x_s in table 1, is computed as the x coordinate of the point closest to the wall where $\Theta > 0.99$. The shock intensity, denoted as I in table 1, is determined as the wall-normal average of the ratio between the pre- and post-shock Mach

https://doi.org/10.1017/jfm.2025.332 Published online by Cambridge University Press

https://doi.org/10.1017/jfm.2025.332 Published online by Cambridge University Press

Case ID	κ_x	ω	A	x_b	x_e	C_L	σ_L	C_D	σ_D	$C_{D,f}$	$C_{D,p}$	C_M	E	x_s	I	ΔC_f	ΔC_D	ΔE	ΔP_n
REF	–	–	–	–	–	0.747	0.12	0.0241	0.21	0.008	0.016	−0.512	31.0	0.47	1.12	–	–	–	–
RREF	–	–	–	–	–	0.664	0.20	0.0221	0.20	0.009	0.013	−0.446	30.0	0.47	1.03	–	–	–	–
C1	36.9	0.0	0.684	0.2	0.78	0.846	0.33	0.0250	0.39	0.007	0.018	−0.570	33.9	0.52	1.11	−37.3	3.5	9.5	−2.2
C2	71.7	0.0	0.684	0.2	0.78	0.826	0.12	0.0243	0.53	0.007	0.017	−0.558	34.0	0.51	1.11	−46.1	0.6	9.8	−2.8
C3	108.7	0.0	0.684	0.2	0.78	0.826	0.31	0.0242	0.47	0.007	0.017	−0.558	34.1	0.51	1.09	−40.6	0.5	10.0	−2.5
C4	254.2	0.0	0.684	0.2	0.78	0.827	0.37	0.0243	0.55	0.007	0.017	−0.559	34.1	0.51	1.11	−30.5	0.7	9.9	−1.1
C5	543.1	0.0	0.684	0.2	0.78	0.826	0.19	0.0242	0.44	0.007	0.017	−0.559	34.1	0.51	1.15	−20.3	0.3	10.2	0.4
C6	108.6	−332.2	0.684	0.2	0.78	0.788	0.29	0.0239	0.34	0.008	0.016	−0.537	32.9	0.49	1.13	−9.2	−0.9	6.3	12.8
C7	108.6	−79.8	0.684	0.2	0.78	0.854	0.25	0.0249	0.35	0.007	0.018	−0.575	34.4	0.53	1.16	−23.7	3.1	10.9	2.7
C8	108.6	−12.7	0.684	0.2	0.78	0.834	0.21	0.0244	0.74	0.007	0.017	−0.562	34.2	0.52	1.12	−37.0	1.2	10.3	−1.6
C9	108.6	12.7	0.684	0.2	0.78	0.827	0.26	0.0243	0.33	0.007	0.017	−0.559	34.0	0.51	1.11	−44.4	0.9	9.6	−2.5
C10/DR	108.6	39.8	0.684	0.2	0.78	0.838	0.19	0.0246	0.23	0.007	0.017	−0.565	34.1	0.52	1.13	−40.8	1.8	10.1	−1.7
R10/DRCL	108.6	39.8	0.684	0.2	0.78	0.750	0.24	0.0211	0.17	0.008	0.013	−0.498	35.5	0.52	1.08	−36.5	−4.4	18.3	–
C11	108.6	58.7	0.684	0.2	0.78	0.797	0.18	0.0241	0.40	0.008	0.016	−0.541	33.0	0.50	1.14	−19.8	0.1	6.5	2.2
C12/DI	108.6	99.6	0.684	0.2	0.78	0.738	0.13	0.0244	0.45	0.008	0.016	−0.506	30.3	0.46	1.12	26.1	1.1	−2.3	14.0
C13	108.6	153.4	0.684	0.2	0.78	0.787	0.16	0.0238	0.36	0.008	0.016	−0.536	33.1	0.49	1.16	−11.1	−1.3	6.8	7.5
C14	108.6	285.2	0.684	0.2	0.78	0.813	0.31	0.0242	0.65	0.008	0.016	−0.552	33.6	0.51	1.12	−12.3	0.3	8.6	9.7
C15	108.6	475.9	0.684	0.2	0.78	0.777	0.33	0.0240	0.36	0.008	0.016	−0.530	32.3	0.49	1.15	−6.3	−0.3	4.4	16.3
C16	110.8	8.6	0.684	0.2	0.78	0.833	0.19	0.0245	0.31	0.007	0.017	−0.562	34.0	0.52	1.13	−41.8	1.5	9.8	−2.4
C17	173.8	25.5	0.684	0.2	0.78	0.812	0.24	0.0239	0.66	0.007	0.017	−0.550	33.9	0.51	1.10	−42.0	−0.8	9.5	−2.3
C18	317.2	64.2	0.684	0.2	0.78	0.819	0.17	0.0241	0.31	0.007	0.017	−0.554	34.0	0.51	1.12	−36.5	−0.2	9.9	−0.9
C19	436.6	94.9	0.684	0.2	0.78	0.825	0.16	0.0241	0.33	0.007	0.017	−0.558	34.3	0.51	1.15	−32.9	−0.2	10.6	−0.2
C20	543.1	126.9	0.684	0.2	0.78	0.820	0.16	0.0241	0.30	0.007	0.017	−0.556	34.1	0.51	1.13	−31.2	−0.2	10.0	1.3
C21	108.6	39.8	0.684	0.2	0.6	0.869	0.10	0.0253	0.34	0.007	0.018	−0.583	34.3	0.53	1.15	−38.1	4.9	10.8	−9.7
C22	108.6	39.8	0.684	0.2	0.4	0.884	0.31	0.0260	0.52	0.007	0.019	−0.591	34.0	0.54	1.15	−33.7	7.8	9.8	−4.4
C23	108.6	39.8	0.684	0.3	0.78	0.741	0.34	0.0240	0.32	0.008	0.016	−0.508	30.9	0.47	1.08	−32.1	−0.7	−0.1	6.1
C24	108.6	39.8	0.684	0.4	0.78	0.713	0.16	0.0243	0.35	0.008	0.016	−0.490	29.3	0.45	1.05	−9.3	0.7	−5.3	12.8
C25	108.6	39.8	0.181	0.2	0.78	0.808	0.16	0.0243	0.37	0.008	0.017	−0.548	33.2	0.50	1.14	−16.6	0.9	7.2	−4.4
C26	108.6	39.8	0.363	0.2	0.78	0.852	0.18	0.0251	0.37	0.007	0.018	−0.574	34.0	0.52	1.16	−28.5	3.9	9.8	−4.6

Table 1. Complete set of simulations. The control parameters are shown in the left part of the table. The middle part reports the aerodynamic coefficients (C_L for lift, C_D for drag and C_M for moment) with the percentage relative standard deviation σ, the friction and pressure components of drag, $C_{D,f}$ and $C_{D,p}$, and aerodynamic efficiency E, shock position x_s and shock intensity I. The rightmost part shows the performance indicators discussed in the text. The relative change of an indicator Φ is defined as the percentage increase with respect to the uncontrolled case (denoted with the '0' subscript), i.e. $\Delta\Phi = 100(\Phi/\Phi_0 - 1)$; in case R10, variations are computed against RREF.

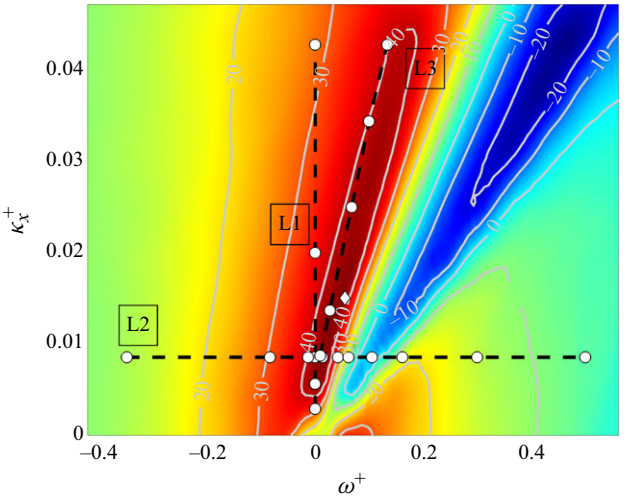


Figure 3. Control parameters for flow cases C1–C20, superposed to the drag reduction map for incompressible plane channel flow (Gatti & Quadrio 2016). The diamond corresponds to case C2 of Quadrio *et al.* (2022). The isolines indicate percentage reduction of friction drag.

numbers. At a given wall distance, the pair of Mach number values is extracted at the two sides of the $\Theta = 0.99$ iso-line, i.e. at the black dots of figure 2.

2.2. *Description of the numerical experiments*

The streamwise-travelling waves (1.1) are characterised by five parameters. Three of them also apply to the canonical case of the plane channel, namely the spatial wavenumber κ_x, the pulsation ω and the amplitude A. Additionally, here, the finite controlled region on the suction side of the aerofoil begins at the position x_b and ends at the position x_e. Following Yudhistira & Skote (2011), an exponential smoothing function acting on a length scale of 0.05 chord units is used at the boundary between active and inactive regions. The space of these five parameters is explored with twenty-nine DNS, listed in table 1, where the control parameters are reported along with some global results to be discussed later.

Case REF corresponds to the baseline unmanipulated flow at incidence angle of 4°. Cases C1 to C20 have a fixed amplitude ($A = 0.684$, equivalent to $A^+ = 11$), and fixed starting point ($x_b = 0.2$) and end point ($x_e = 0.78$) of the forcing, as in Quadrio *et al.* (2022). These cases are depicted by dots in figure 3, where the drag reduction map for the incompressible channel flow at $Re_\tau = 200$ (Gatti & Quadrio 2016) is reported. The first subset of cases lies on the vertical line L1 at $\omega = 0$, corresponding to steady forcing; the second subset lies on the horizontal line L2 at constant wavelength, crossing both drag-reducing and drag-increasing regions of the parameter space; the third subset lies along the oblique line L3, corresponding to the ridge of maximum drag reduction in incompressible channel flow. Additional cases from C21 to C26 are designed to understand the effects of the remaining control parameters (x_b, x_e and A). One simulation (labelled as R10 in table 1) modifies one of the best-performing cases (namely C10) by reducing the incidence angle from 4° to 3.45°, in such a way that the controlled aerofoil yields the same lift of the original uncontrolled case. Case RREF is the corresponding unmanipulated simulation at reduced incidence.

In the remainder of the paper, special attention will be paid to cases C10 (one of the best performers), C12 (the only case yielding drag increase) and R10 (same as C10 but

https://doi.org/10.1017/jfm.2025.332 Published online by Cambridge University Press

with reduced incidence). For readability, they will be renamed DR (drag reduction), DI (drag-increase) and DRCL (drag reduction at constant lift).

3. Aerodynamic performance

In this section, we consider the effectiveness of StTWs in terms of modification of the force and momentum coefficients of the aerofoil, which are connected to changes in the distribution of the wall stresses along the chord. Last, the energetic performance of StTWs is discussed.

When discussing changes induced by the forcing, the variations, indicated with the symbol Δ, are consistently defined as a percentage increase with respect to the reference case.

3.1. *Force and moment coefficients*

Aerodynamic forces and moments derive from the integrated distributions of the projected wall friction and pressure, whose coefficients are defined as

$$C_f(x) = \frac{2\tau_w(x)}{\rho_\infty U_\infty^2}, \qquad C_p(x) = \frac{2\left[p_w(x) - p_\infty\right]}{\rho_\infty U_\infty^2}, \tag{3.1}$$

where τ_w and p_w are the mean wall-shear stress and the mean wall pressure, respectively, obtained after averaging in time and along the spanwise direction.

The mean aerodynamic force $\boldsymbol{F}$ is

$$\boldsymbol{F} = \oint_S \left[\tau_w \hat{\boldsymbol{t}} - p_w \hat{\boldsymbol{n}}\right] \mathrm{d}S = \frac{1}{2}\rho_\infty U_\infty^2 \oint_S \left[C_f \hat{\boldsymbol{t}} - C_p \hat{\boldsymbol{n}}\right] \mathrm{d}S, \tag{3.2}$$

where $\hat{\boldsymbol{t}}$ and $\hat{\boldsymbol{n}}$ are the local unit vectors respectively tangent and normal to the wall, and S is the wing surface. Here, $\boldsymbol{F}$ is conventionally decomposed into lift L and drag D components, respectively normal and parallel to the free stream velocity. The aerodynamic pitching moment M_{TE} with respect to the trailing edge is determined as

$$M_{TE} = \hat{\boldsymbol{z}} \cdot \oint_S \boldsymbol{r} \times \left[\tau_w \hat{\boldsymbol{t}} - p_w \hat{\boldsymbol{n}}\right] \mathrm{d}S, \tag{3.3}$$

where $\hat{\boldsymbol{z}}$ is the unit vector in the spanwise direction and $\boldsymbol{r}$ is the distance vector from the trailing edge. The values of the force and momentum coefficients C_L, C_D and C_M are reported in table 1.

Figure 4(*a*) shows the distribution of the friction coefficient along the chord. The reference case (black line) overlaps with the nominally identical one computed by Quadrio *et al.* (2022), with minor discrepancies near the leading edge due to differences in the numerical procedure adopted. The plot highlights some important flow features, as the local peak of C_f at $x = 0.1$ due to tripping, the local reduction under the shock wave (whose position is indicated with the vertical dashed line) and the near zero values at the trailing edge on the suction side. To analyse the effects of wall actuation on friction, the reference case is compared with cases DR, DRCL and DI. Direct effects of control are observed on the suction side only, where it is applied. In terms of friction, the effects of StTWs are as expected: after the forcing is applied (i.e. for $x > 0.2$), friction decreases (or increases, for DI), becoming mildly negative past the shock for cases DR and DRCL. Simulation DRCL with modified incidence is very similar to DR on either side of the aerofoil, with exception of the region right upstream of the shock, where friction is slightly higher. The shock moves downstream in the drag-reducing cases, whereas it moves upstream for DI. Figure 4(b) shows the distribution of the pressure coefficient. In the REF

https://doi.org/10.1017/jfm.2025.332 Published online by Cambridge University Press

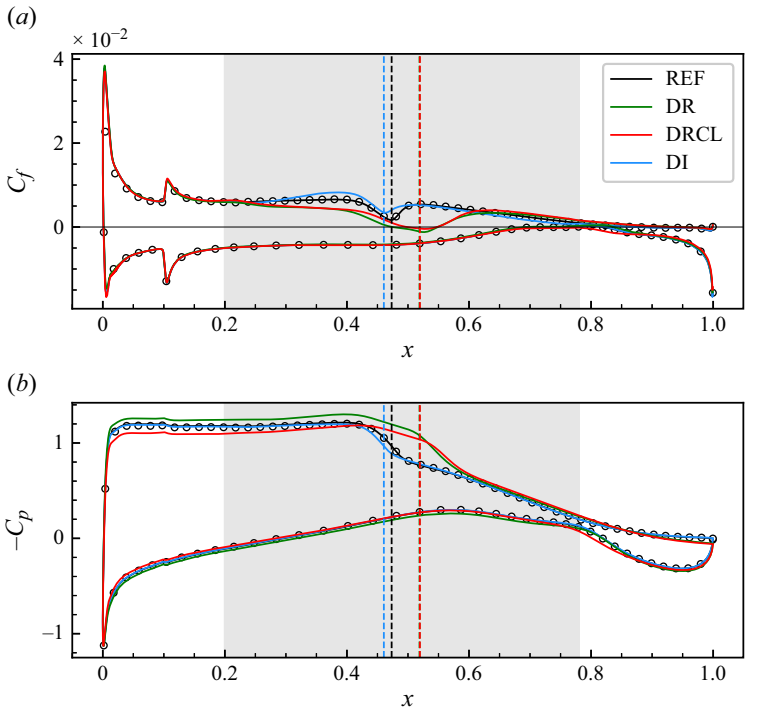


Figure 4. Distributions of (a) friction coefficient (C_f) and (b) pressure coefficient (C_p, along the aerofoil. Dots are from the reference simulation by Quadrio *et al.* (2022) and overlap with the present REF case. The vertical lines mark the shock position for each case (note that DR and DRCL overlap); the grey area indicates the active region (on the suction side only).

case, the sudden flow expansion at the leading edge is followed by a plateau where, by design, the aerofoil achieves nearly zero pressure gradient. Further downstream, the mildly negative slope of C_p reveals the presence of a shock. The wall pressure distributions for DR and DRCL do not coincide as a consequence of the different incidence, while the position of the shock across the two cases is unchanged. Case DRCL provides the same lift as the reference case, although its wall pressure remains higher (hence with a lower C_p) than the reference simulation in the first 40 % of the chord: StTWs displace the shock downstream and the supersonic low-pressure region is wider.

Figure 5 shows the local friction and pressure contributions to the drag coefficient ($C_{d,f}$ and $C_{d,p}$, respectively, whose integrals are presented in table 1 as $C_{D,f}$ and $C_{D,p}$). The distribution of $C_{d,f}$ is very similar to the friction coefficient (depicted in figure 4) on the suction side (panel a), as in this region, the wall is rather flat and aligned to the free stream. The effect of wall actuation on the pressure side, shown in panel (b), is instead rather small, with minor differences close to the trailing edge associated with different values of the angle of attack. As for $C_{d,p}$ (panels c and d), all the distributions essentially overlap. However, one should bear in mind the different magnitude of the contributions of pressure and friction to the overall drag, which renders pressure changes significant.

This is emphasised in figure 6, where differences between the controlled and uncontrolled cases at the two incidence angles of cases DR and DRCL are shown. On the suction side (panels a and c), the frictional contribution only shows small variations, whereas the pressure contribution exhibits significant changes close to the shock, around the mid-chord. In that region, control yields positive variations of $C_{d,p}$ and contributes to

https://doi.org/10.1017/jfm.2025.332 Published online by Cambridge University Press

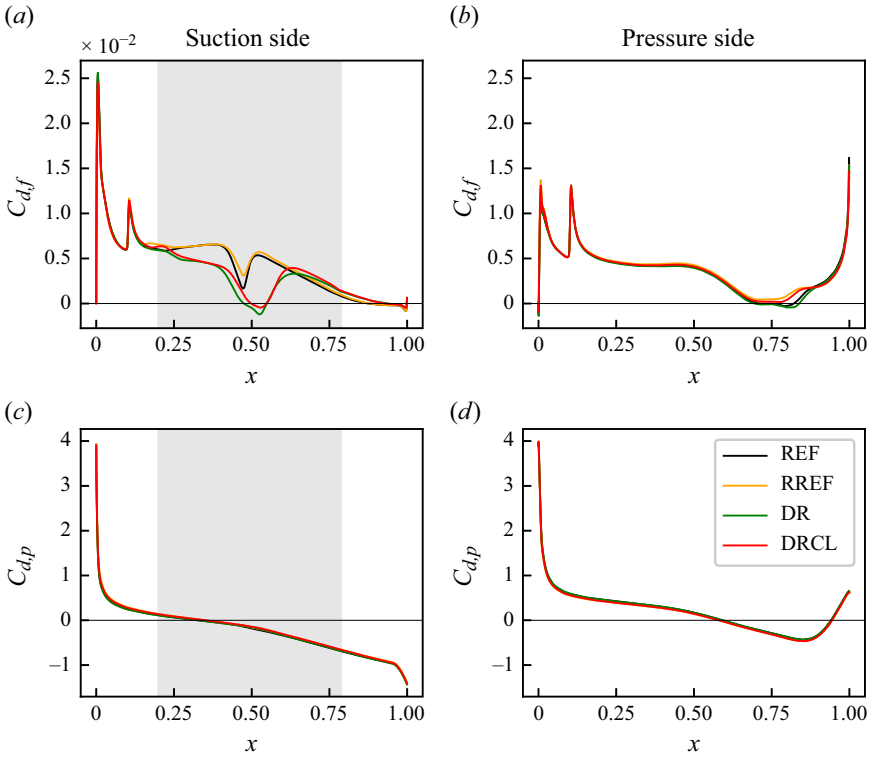


Figure 5. (*a,b*) Local friction ($C_{d,f}$) and (*c,d*) pressure ($C_{d,p}$) contributions to C_D on the (*a,c*) suction side and (*b,d*) pressure side of the aerofoil. The grey area highlights the active region (on the suction side only).

drag increase. This positive contribution is smaller at the lower incidence $\alpha = 3.45°$, as the shock is weaker (see table 1). Panels (*b*) and (*d*) show that changes on the pressure side are instead smaller, and do not depend on incidence.

Having isolated the effects of the reduced incidence angle from those directly ascribed to StTWs, some conclusions can be drawn: (i) StTWs always reduce friction drag, except for those combinations of control parameters for which drag increase is expected from channel flow information; (ii) StTWs tend to increase pressure drag, as a result of shock strengthening; (iii) a smaller angle of attack reduces the pressure contribution to the drag force, at least within the range of values considered here, with a less significant effect on the friction contribution; (iv) although the friction and pressure contributions to drag have different magnitudes, the relative control-induced variations are comparable.

3.2. *Effects of the control parameters*

The performance of StTWs as a function of the control parameters is well understood in the canonical plane channel flow, where drag is entirely due to friction, and the mean friction is constant along the channel; comprehensive information exists which maps the control parameters into drag reduction figures. Furthermore, even if compressibility is taken into account, the reduction of the skin-friction coefficient (and the net power gain) is essentially unchanged as long as the framework remains that of the plane channel flow, as demonstrated by Gattere *et al.* (2024). Hence, at least locally, the effects of StTWs on the skin-friction over the transonic wing could be derived directly from the canonical

https://doi.org/10.1017/jfm.2025.332 Published online by Cambridge University Press

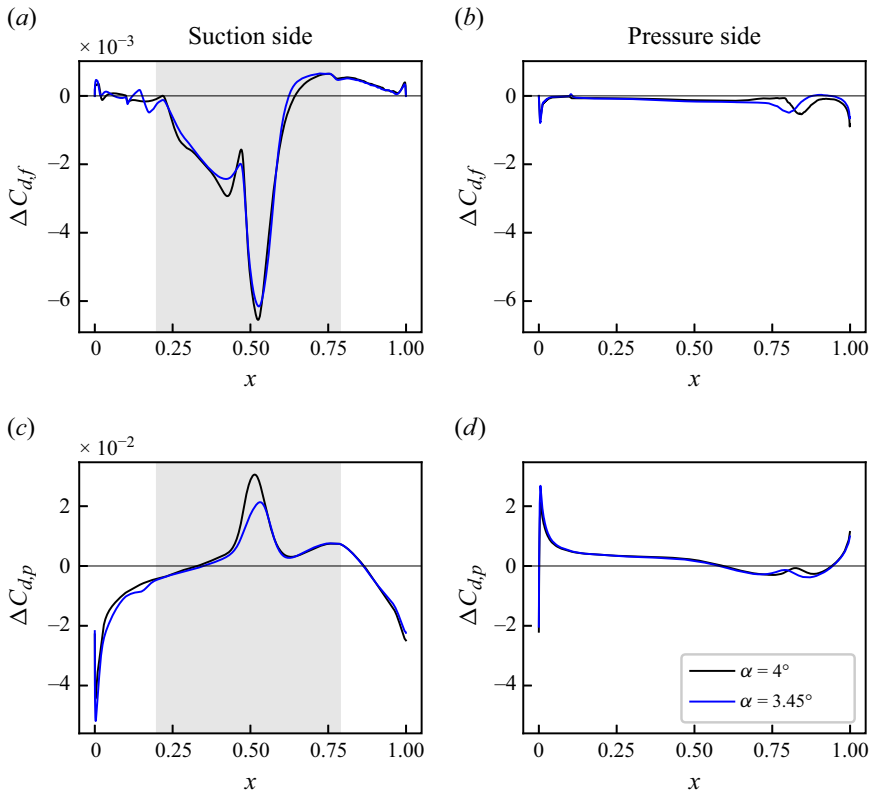


Figure 6. Local difference of (*a,b*) frictional ($\Delta C_{d,f}$) and (*c,d*) pressure ($\Delta C_{d,p}$) contributions to the drag coefficient on the suction and pressure sides of the aerofoil. The black lines express the differences between DR and REF cases, whereas the blue lines are obtained comparing cases at lower incidence DRCL and RREF.

channel flow. However, the same does not apply on a global level, since the mean flow properties vary strongly along the streamwise direction due to wall curvature, adverse pressure gradient and the shock wave.

One can define the relative local reduction of the friction coefficient as

$$\Delta C_f(x) = 100\frac{C_f(x) - C_{f,0}(x)}{C_{f,0}(x)}; \tag{3.4}$$

this quantity varies because of changes of C_f itself, and because of the presence of the gradual spatial evolution after x_b of the control effect (Skote 2012). Figure 7 plots $\Delta C_f(x)$ for flow cases DR and DRCL, limited to the portion of the suction side where forcing is active. The variations of C_f along the chord are significant, thus making it difficult to distil the function $\Delta C_f(x)$ into a single number to compare with the case of the channel flow. However, one can identify a portion of the curve (for example, $x \leqslant 0.4$) over which changes in friction can be attributed mainly to wall actuation.

Hence, we consider the value of ΔC_f at $x = 0.4$ as a surrogate measure of frictional drag reduction and define the viscous units with the friction velocity measured at $x = 0.4$. A detailed analysis of how this choice affects the comparison with the case of channel flow is presented in Appendix A, together with law-of-the-wall plots of the mean streamwise velocity profiles extracted at $x = 0.4$.

In figure 8, we compare the values of friction drag reduction $-\Delta C_f$ at $x = 0.4$ for the simulations C1–C20 at constant forcing intensity A with data for the incompressible

https://doi.org/10.1017/jfm.2025.332 Published online by Cambridge University Press

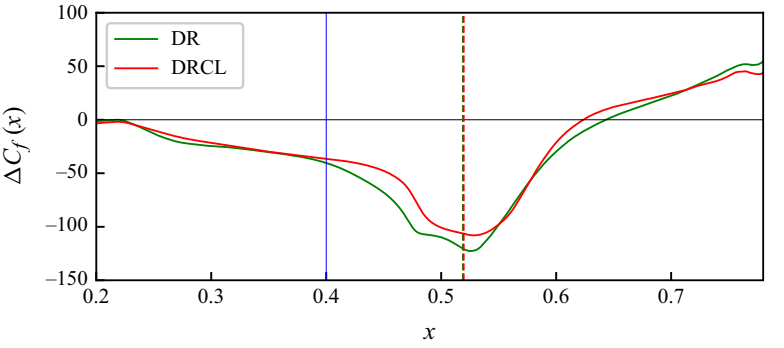


Figure 7. Relative local change of the friction coefficient ($\Delta C_f(x)$) on the portion of the suction side where control is active, for cases DR and DRCL compared with case REF. The vertical blue line at $x = 0.4$ shows where frictional drag reduction is evaluated, whereas the two (nearly coincident) vertical dashed lines display the positions of the shock.

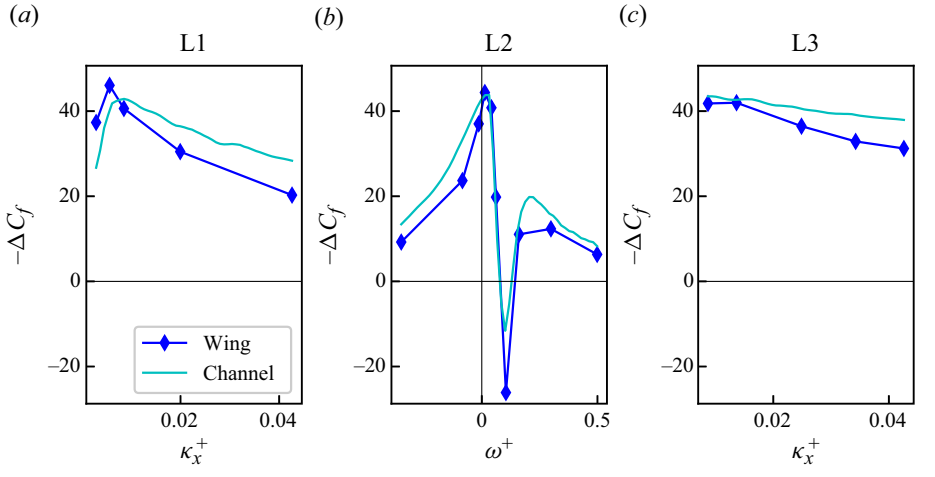


Figure 8. Comparison of local reduction of friction coefficient ($-\Delta C_f$) for flow cases C1–C20, across lines L1, L2 and L3 in figure 3 and incompressible channel flow at $Re_\tau = 200$ (Gatti & Quadrio 2016).

channel flow at $Re_\tau = 200$ (Gatti & Quadrio 2016), properly interpolated to precisely match the control parameters of each case. While the magnitudes of ΔC_f should be regarded qualitatively for the reason discussed above, the trends are remarkably similar. In particular, in both cases, the global maximum of drag reduction is found for slow, forward-travelling waves.

Relative variations of the force and momentum coefficients of the aerofoil for flow cases C1–C20 are reported in figure 9. Perhaps surprisingly, the drag coefficient is found to undergo little changes, with at most a reduction of approximately 1 %, as a consequence of wall actuation; in addition, in some cases, it even increases slightly. As expected, changes in the pitching moment, which is mainly controlled by pressure, are analogous to changes in C_L.

Figure 10 displays the friction contribution to the total drag combined with the friction drag reduction. StTWs generally decrease the friction contribution to the overall drag, with the exception of the friction-drag-increasing case DI. Whereas in the reference simulation friction is responsible for 34 % of the entire drag, this fraction reduces to 29 % in the presence of wall actuation. The minor changes observed in C_D imply that the relationship

https://doi.org/10.1017/jfm.2025.332 Published online by Cambridge University Press

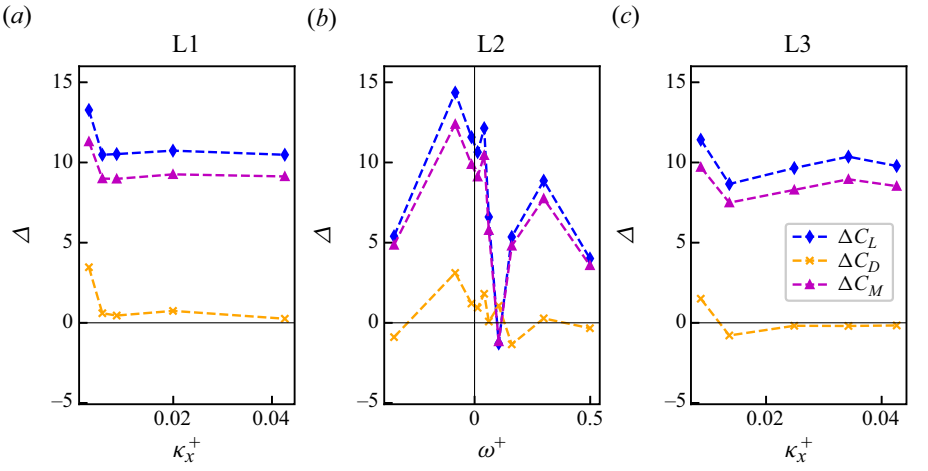


Figure 9. Relative variations of lift (ΔC_L), drag (ΔC_D) and pitching moment (ΔC_M) coefficients, for the cases C1–C20 across lines L1, L2 and L3 of figure 3.

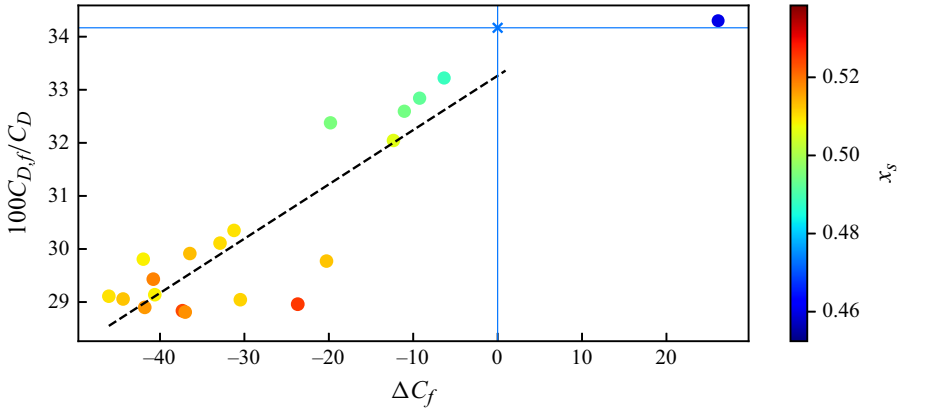


Figure 10. Percentage friction contribution to drag ($100C_{D,f}/C_D$), as a function of the friction drag changes (ΔC_f) for cases C1–C20 across lines L1, L2 and L3 of figure 3. The colour of each data point encodes the shock position. The cross indicates the reference case, while the dashed line is a linear regression of the data for $\Delta C_f < 0$.

between ΔC_f and $C_{D,f}$ is close to linear. The shock wave is located at $x_s = 0.47$ in the reference case, and a connection between a large local friction reduction and a downstream displacement of the shock is clearly visible. The further the shock is delayed towards the trailing edge, the stronger the expansion on the suction side of the aerofoil. Since the post-shock conditions to be matched are approximately the same (see C_p in figure 4), we can conclude that the shock intensity does depend on the shock position, as can be seen from the parameters listed in table 1. Hence, a stronger shock leads to a larger pressure contribution to the aerodynamic coefficients.

3.3. *Net savings*

As discussed in § 1, assessing the effectiveness of active flow control strategies requires to estimate the energy expenditure for the actuation. In canonical flows, in which drag consists only of friction, one may want to exploit the positive effect of friction-reducing control to improve the balance between performance (e.g. the mass flow rate in channel

https://doi.org/10.1017/jfm.2025.332 Published online by Cambridge University Press

flow or the pressure losses through the duct) and the related cost, the pumping power. However, infinite ways exist to modify such balance, the two extreme cases being maximisation of performance for given cost or minimisation of cost for given performance. In a plane channel flow (Frohnapfel, Hasegawa & Quadrio 2012) the two approaches are referred to as constant-pressure-gradient comparison (CPG, whereby the pumping force per unit volume is unchanged and the flow rate can change) and the constant-flow-rate comparison (CFR, whereby the flow rate is unchanged and the pumping force per unit volume can change). A similar line of reasoning applies to the present case, but the definition of costs and benefits is less obvious. As we have seen, the main effect of wall actuation is to increase lift; however, lift is a poor indicator of performance. In fact, in cruise flight, the wing is bound to always generate the same lift force for balancing the aircraft weight.

In analogy with the CFR comparison procedure, an increase of lift can be exploited to reduce the angle of attack, thus aiming at cost minimisation for unchanged performance. Let $\Pi_0 = D_0 U_\infty$ be the nominal power required for flying the aircraft at constant speed U_∞, with D_0 the drag force in the uncontrolled configuration. One can define the net rate of change of the cruise flight power requirement (ΔP_n) as the ratio between the reduction of flight power (incremented by the control power) and the reference power:

$$\Delta P_n = \frac{(\Pi + \Pi_c) - \Pi_0}{\Pi_0}, \tag{3.5}$$

where $\Pi = D\,U_\infty$ is the power required to fly the wing at the same speed U_∞ in the controlled configuration. The subscript n in ΔP_n emphasises that the power change is a net balance that accounts for the extra power Π_c required by the active forcing. At the numerator of (3.5), the power reduction $-(\Pi - \Pi_0)$ is obviously linked to the drag reduction $-(D - D_0)$, where the drag D is the drag obtained in a configuration yielding the same lift of the reference case. Finally, the control power Π_c is the power transferred from the StTWs to the fluid, assuming unitary efficiency $\gamma = 1$ of an ideal actuator, as alway done in numerical studies. Values for γ are typically not provided by experimental studies (e.g. Bird *et al.* 2018; Marusic *et al.* 2021; Fumarola, Santer & Morrison 2024; Knoop *et al.* 2024) where StTWs were tested; these studies either overlook the net savings or simply assume ideal efficiency. While Gatti *et al.* (2015) mention a large value of $\gamma = 0.7$ for their electro-mechanical actuator for the spanwise oscillating wall, the typical proof-of-principle experiment employing simple mechanical actuators has low efficiencies: for example, actuation power reported by Auteri *et al.* (2010) for their mechanical implemention of StTWs is 1528 mW, against an ideal control power of 2.1 mW ($\gamma = 0.0014$).

The drag D required to evaluate (3.5) is derived from the lift increase ΔL brought about by wall actuation via the following procedure: (1) the lift curve $C_L(\alpha)$ of the uncontrolled wing is used to determine the reduced incidence angle required to recover the original lift when the control is applied (hence, causing the variation ΔC_L available in table 1); (2) the drag curve $C_D(\alpha)$ of the uncontrolled wing is used to interpolate drag at the reduced incidence (the presence of forcing is not accounted for yet); (3) the drag coefficient at the reduced incidence is modified to account for the variation ΔC_D (available in table 1) caused by the direct action of StTWs.

Points (1) and (2) above require the polar curve of the V2C aerofoil, which is impractical to obtain via DNS, and has been computed with RANS instead. In particular, the open-source compressible RANS solver SU2 v.7.5.1 is used, with differential operators at second-order accuracy, and free stream conditions matching those of the DNS. The central Jameson–Schmidt–Turkel scheme (Jameson, Schmidt & Turkel 1981) has been employed for the convection terms, with the default Venkatakrishnan slope limiter (Venkatakrishnan 1995) employed to preserve monotonicity near shocks. The weighted least squares method

https://doi.org/10.1017/jfm.2025.332 Published online by Cambridge University Press

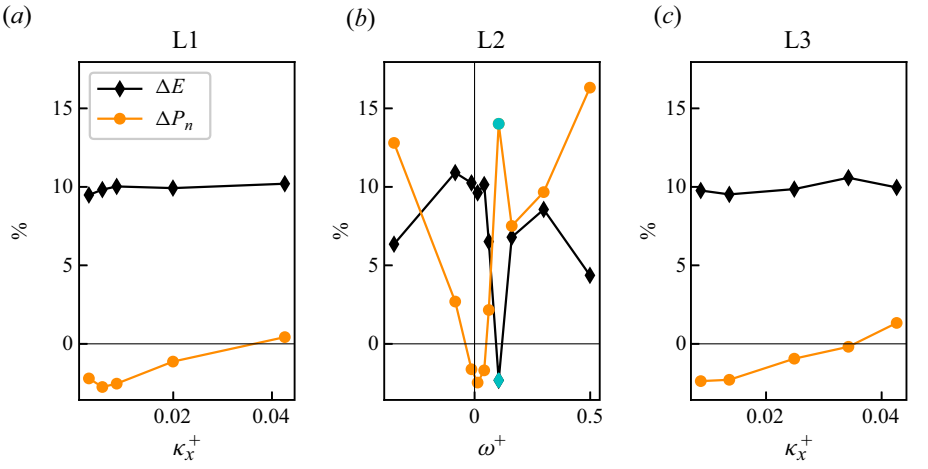


Figure 11. Changes in aerodynamic efficiency (ΔE) and net power (ΔP_n) for cases C1–C20 across lines L1 (standing wave), L2 (fixed κ_x) and L3 (ridge of maximum drag reduction) of figure 3. The cyan markers highlight case DI.

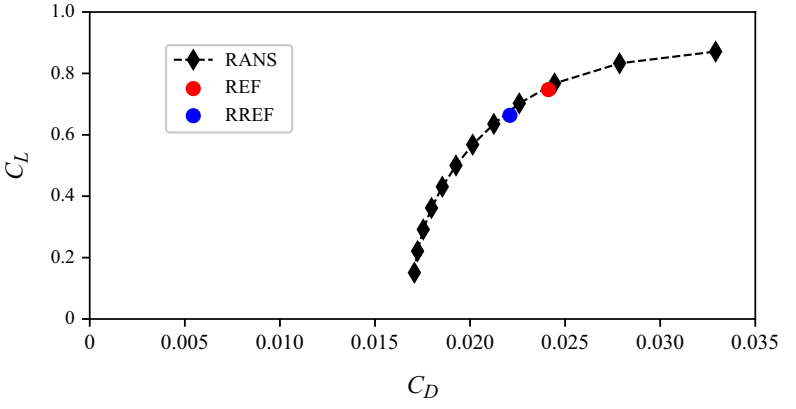


Figure 12. Polar curve of the V2C aerofoil.

is employed for discretising the gradient operator involved in the viscous terms. Turbulence is modelled through the wall-resolved Spalart–Allmaras model (Spalart & Allmaras 1992). The grid is an unstructured, two-dimensional circular mesh with radius of 100 chords, consisting of 429 100 volume elements. It features an orthogonal prism layer refinement at the aerofoil surface, which guarantees element orthogonality and a wall resolution of approximately one viscous unit just ahead of the shock. To avoid additional uncertainty, no transition modelling has been employed. The simulations are run until the relative change of drag coefficient is smaller than 10^{-8}. The pseudo time-stepping required to reach convergence of the steady simulation is performed with implicit Euler. The RANS-based polar is shown in figure 12, together with the datapoints computed with DNS.

Results of the procedure in terms of ΔP_n are presented in figure 11: we recall that under the convention employed in this paper, positive ΔP_n implies more power required in the controlled case, hence power loss. Figure 11 shows that changes of aerodynamic efficiency are generally positive with ΔE typically increasing by 10 % on average and up to 30 %. An exception is case DI, highlighted by the cyan markers, which yields drag increase and consequently reduced efficiency. Against the improved efficiency, the required power

https://doi.org/10.1017/jfm.2025.332 Published online by Cambridge University Press

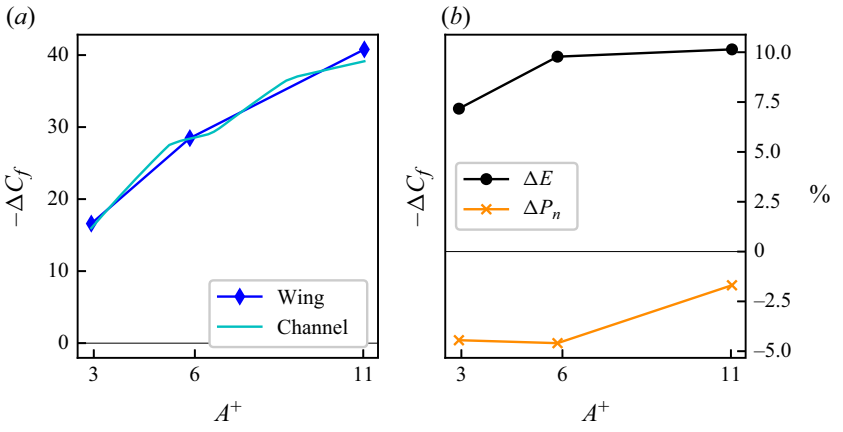


Figure 13. Performance metrics for flow cases with different forcing amplitude A^+: C25 ($A^+ \approx 3$), C26 ($A^+ \approx 6$) and DR ($A^+ \approx 11$). (*a*) Changes in C_f, compared with incompressible channel flow data; (*b*) changes in the aerodynamic efficiency and net savings.

does not always decrease, being basically unchanged in a few cases and increased in the remaining ones. This is an expected result that parallels the incompressible channel flow, where the power balance at this rather large forcing amplitude is unfavourable. As in the channel, the net balance is found to be best for slow, forward-travelling waves (Quadrio *et al.* 2009). These figures are minimally altered when using the RANS datapoint for the reference state, which yields a slightly better (up to 1.4 % extra) power saving.

Extent and position of the active region are two control parameters with no counterpart in the homogeneous channel flow. Simulations C21–C24 have been performed to quantify how the baseline values of $x_b = 0.2$ and $x_e = 0.78$ considered by Quadrio *et al.* (2022) affect the results. Specifically, in flow cases C21 and C22, the end point of the actuated region is moved upstream for fixed x_b, whereas in cases C23 and C24, the origin is shifted downstream for a fixed x_e. In all cases, the active area is reduced, yet the results listed in table 1 show that ΔC_f is minimally altered when x_e is shifted upstream; in contrast, moving x_b downstream adversely affects ΔC_f, $x_b = 0.4$ being the worst case. The best choice for increasing the aerodynamic efficiency seems thus to be $x_b = 0.2$ and $x_e = 0.6$, yielding $\Delta P_n = -9.7$ %, which is the best value obtained among all the DNS performed at $\alpha = 4°$.

It is well known that the energetic efficiency of StTWs varies with the forcing amplitude A in the case of flow over plane walls. This dependence is here verified in flow cases C25 and C26, which replicate case DR with lower forcing amplitudes. The results are presented in figure 13, in which panel (*a*) shows the resulting changes of ΔC_f compared with the incompressible channel flow data, interpolated from the database by Gatti & Quadrio (2016), while panel (*b*) displays ΔE and ΔP_n. Just as for incompressible channels, the friction drag reduction decreases for smaller forcing amplitudes. The agreement, both in qualitative and quantitative terms, between the curves of wing and plane channel flow is remarkable. Interestingly, the improvement of the aerodynamic efficiency (panel *b*) does not follow ΔC_f, and halving the control intensity from $A^+ \approx 11$ to $A^+ \approx 6$ does not decrease ΔE. We find a minumum value of ΔP_n for the case C27, corresponding to $A^+ = 6$. This is a significant analogy with the incompressible channel flow, in which maximum efficiency is obtained for $A^+ \approx 5$ (Quadrio *et al.* 2009), as the power cost grows quadratically with A.

Finally, it is important to stress that in this specific application, the true benefits of StTWs hinge upon the increase of aerodynamic efficiency, and become more significant

https://doi.org/10.1017/jfm.2025.332 Published online by Cambridge University Press

when the entire aircraft is considered instead of the wing alone. Therefore, for case DR, we replicate the line of reasoning followed by Quadrio *et al.* (2022) and extrapolate the potential saving to a complete aircraft. Specifically, we consider the same wing-body configuration, i.e. the 'DLR-F6' (Laflin *et al.* 2005), at the reference uncontrolled conditions of $M = 0.75$, $Re_\infty = 3 \times 10^6$ and $\alpha_0 = 0.52°$. Aircraft information is extracted from the dataset available online at https://aiaa-dpw.larc.nasa.gov/Workshop2/DPW_forces_WB_375.

The simplifying hypotheses adopted are the following:

(i) the wing-generated lift is the only contributor to the overall lift of the aircraft: the fuselage and the tail do not contribute (hence, no additional lift sources are considered);
(ii) the non-lift-induced drag (i.e. the drag that is computed via this procedure) corresponds to one-third of the overall drag;
(iii) the aerodynamic coefficients and the control effects are constant along the wingspan, and do not change with Re_∞ and M_∞, so that results obtained for the wing section are extended to the whole wing without finite-wing corrections;
(iv) the slopes of the curves $C_L - \alpha$ and $C_D - \alpha$ are not affected by the control;
(v) the actuated surface is one-fourth of the wing surface and one-twelfth of the whole aircraft surface.

Under these assumptions, one can estimate how StTWs as in case DR would improve the drag coefficient of the entire aircraft. The procedure adopted, which resembles that described above to obtain ΔP_n, has already been presented by Quadrio *et al.* (2022) and therefore is not reported here in detail. The smaller angle of attack in cruise flight, made possible by StTWs, translates into a decrease of the aircraft drag coefficient of $\Delta C_D = -8\,\%$. This reduction is then augmented by the effect of the StTWs at the reduced angle of attack (see table 1), which yields the additional benefit of $\Delta C_D = -4.4\,\%$. From the energetic viewpoint, the theoretical $\gamma = 1$ control power Π_c required by the actuation at unitary efficiency is 0.4 % of the overall flight power, yielding a nominal net gain of 12 %. While a suitable actuator for StTWs is missing, it may be interesting to mention that this combination of net savings and required power translates into the minimum value of efficiency required by an actuator to provide a positive power gain. The mimimum efficiency is simply the inverse of the maximum gain discussed by Kasagi *et al.* (2009). If the requirement for net savings is reformulated via (3.5) for the complete aircraft and for non-unitary control efficiency as

$$\Delta P_n = \frac{(\Pi + \Pi_c/\gamma) - \Pi_0}{\Pi_0} \leqslant 0, \tag{3.6}$$

the control performance is such that an actuator efficiency as low as $\gamma = 0.045$ is enough to yield a net power gain.

4. Flow organisation

After the description of the effect of StTWs in global terms through the aerodynamic coefficients, the focus is shifted here on the interaction between the forcing (or, more precisely, the reduced levels of friction brought about by it) and the turbulent boundary layer with the shock wave.

https://doi.org/10.1017/jfm.2025.332 Published online by Cambridge University Press

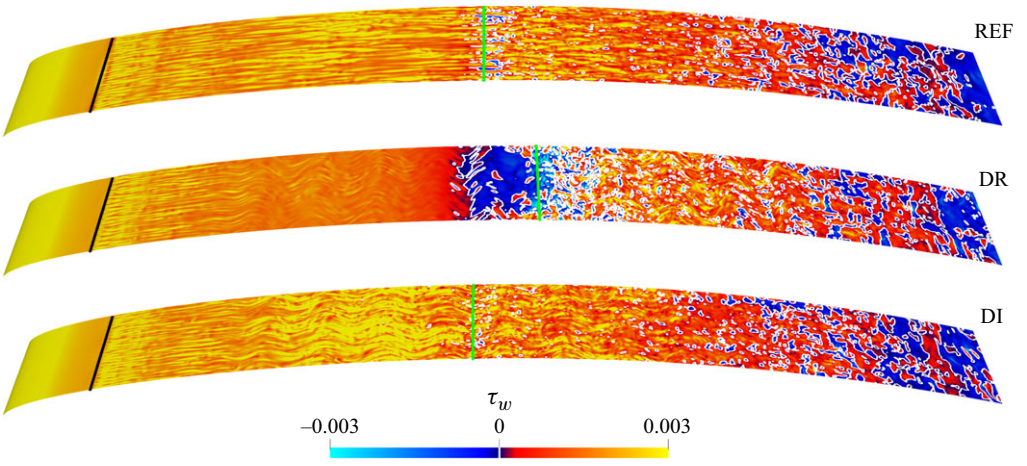


Figure 14. Instantaneous wall-shear stress on the suction side of the aerofoil. The black lines indicate the position of the tripping and the green lines denote the position of the shock in the three cases; the white contours correspond to $\tau_w = 0$.

4.1. *Boundary layer*

Figure 14 shows a comparative view of the instantaneous wall-shear stress (τ_w) on the suction side of the wing for the REF, DR and DI flow cases. Close to the leading edge, the flow is laminar up to the tripping location, where streaks of high- and low-speed fluid, whose footprints are visible at the wall, begin to form due to the imposed transition. In the reference case, turbulent structures are convected downstream towards the shock, where the strong adverse pressure gradient slows the flow and changes their shape. The wall-shear stress remains positive on average around the shock, while showing instantaneous, locally negative spots. In case DR, the streaks are similar to the reference case right past the tripping point, but the forcing affects their dowstream development past $x_b = 0.2$. Further downstream, where the influence of the shock is stronger, mild flow reversal develops upstream of the shock position, as made evident by the large region with negative wall shear. The observed flow reversal however is likely connected with the limited Reynolds number of the present configuration. In flow case DI, in which wall actuation is ineffective and even yields local increase of τ_w, the near-wall cycle is strengthened, yielding turbulence intensification and higher friction. Here, the streamwise modulation of the flow induced by wall actuation is clearly visible, both upstream and downstream of the shock. According to Quadrio *et al.* (2009), this is an indicator that spanwise forcing is operating far from the optimal conditions.

The reversed flow region around the shock is further explored in figure 15, where its length and position, colour-coded with $-\Delta C_f$, are plotted against the position of the shock wave x_s for cases with constant control extension (i.e. cases C1–C20 and C25–C26). Figure 15 highlights a dependence between the length of the separated region and the position of the shock wave, further influenced by the skin-friction reduction rate; note that this relationship is quite robust, as the plot includes also results with different control amplitude (cases C25–C26). In fact, we observe that the reversed flow area consistently includes the shock and all cases with large ΔC_f feature long separation bubbles. The longest reversed flow region (approximately 9 % of the chord) is found in case C2, which also achieves the largest friction drag reduction ($\Delta C_f = -46$ %). Conversely, case DI (drag-increase) and case C15 (which has the smallest positive $-\Delta C_f$) exhibit no flow separation and the shock resides further downstream, similarly to the unactuated case.

https://doi.org/10.1017/jfm.2025.332 Published online by Cambridge University Press

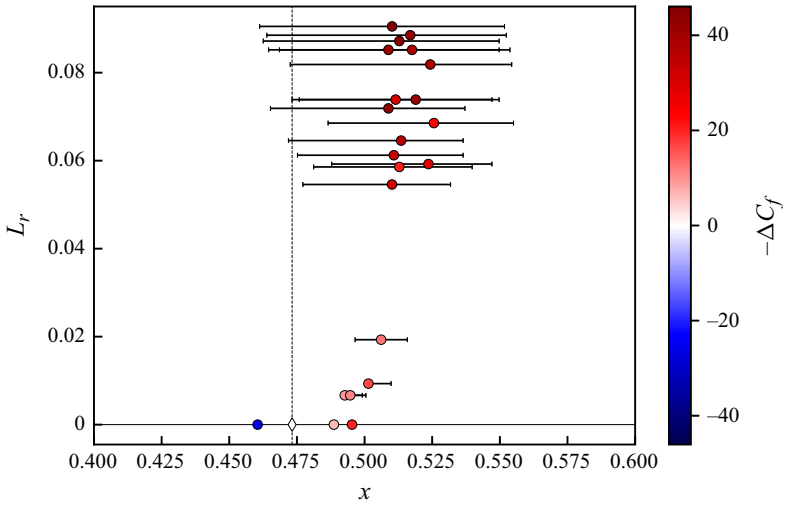


Figure 15. Shock position (dots) and extent of the reverse-flow region (horizontal bars). The vertical dashed line marks the shock position in the reference case. The dots are coloured according to the skin-friction reduction rate $-\Delta C_f$. The white diamond corresponds to the unmanipulated flow.

The compressible boundary layer thicknesses δ^*, θ and shape factor H are are shown in figure 16. It is well known that the local wall-shear stress is linked to streamwise variations of the boundary layer thicknesses δ^* and θ via the von Kármán integral equation. They are computed as done by Xu, Ricco & Duan (2023):

$$\delta^* = \int_0^\infty \left(1 - \frac{\overline{\rho}\,\widetilde{u}}{\rho_e U_e}\right) \mathrm{d}\eta, \qquad \theta = \int_0^\infty \left(1 - \frac{\widetilde{u}}{U_e}\right) \frac{\overline{\rho}\,\widetilde{u}}{\rho_e U_e} \mathrm{d}\eta, \qquad H = \delta^*/\theta, \quad (4.1)$$

where $\bar{\cdot}$ and $\widetilde{(\cdot)}$ denote the temporal and Favre-averaging operators, and the subscript 'e' denotes a quantity at the edge of the boundary layer. The edge of the boundary layer is identified with the wall-normal position at which the tangential velocity reaches 99 % of the maximum local tangential velocity.

As long as the wall curvature is limited, a reduction in the wall-shear stress should be associated with a reduction in the growth rate of the momentum thickness. This is indeed observed in the curve corresponding to case DR in figure 16(*b*). Moreover, the pre-shock adverse pressure gradient region in case DR is wider, the shock moves downstream significantly and the deceleration required to bring the flow back to the trailing edge conditions is stronger: the larger velocity defect is reflected in a larger displacement thickness, which is indeed seen to grow significantly at $x \simeq 0.5$. The combination of these two effects yields a higher shape factor in flow case DR, which indicates that the boundary layer is more prone to flow reversal. The drag-increasing case DI differs in that near the shock, both δ^* and θ (panels *a* and *b*, respectively) slightly grow due to the adverse pressure gradient, hence the shape factor, panel (*c*), does not change significantly. The streamwise pressure gradient is shown in figure 16(*d*). For the reference and drag-increasing cases, the peak of $\partial C_p/\partial x$ corresponds to the shock position, whereas for flow case DR, the peak lies distinctly downstream of the shock, with approximately the same magnitude. A barely discernible secondary peak is also found upstream of the shock ($x \approx 0.47$), the two peaks approximately marking the start and the end of the flow reversal.

https://doi.org/10.1017/jfm.2025.332 Published online by Cambridge University Press

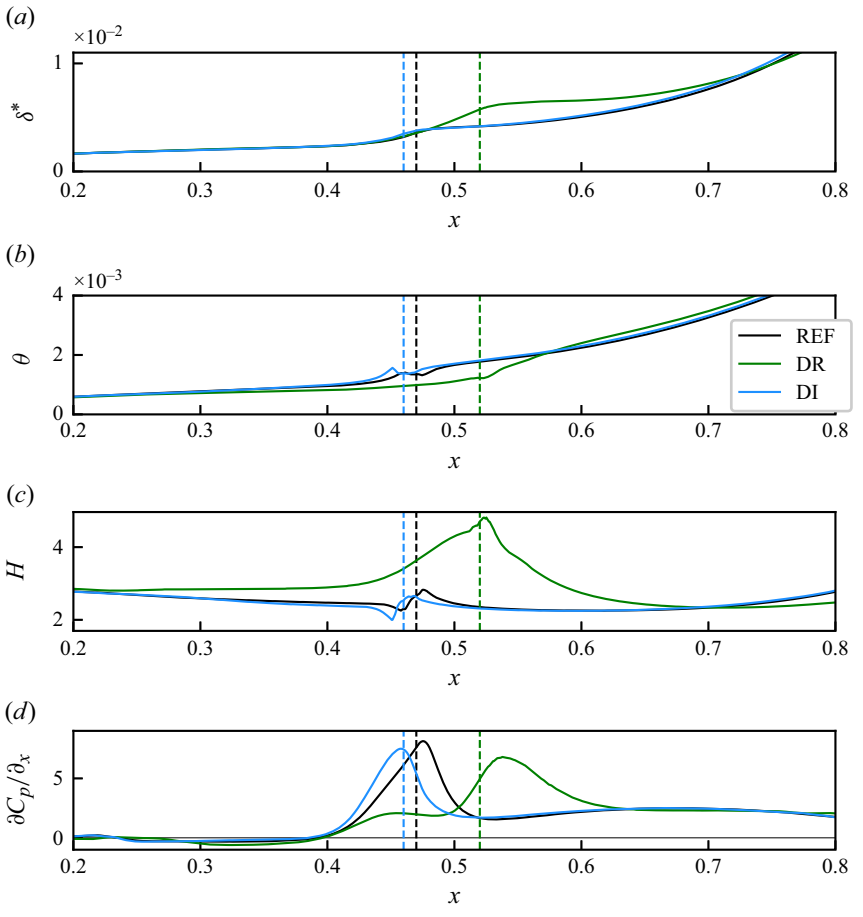


Figure 16. Distribution of integral boundary layer parameters and pressure gradient across the actuated region on the suction side for the REF, DR and DI flow cases: (*a*) displacement thickness (δ^*); (*b*) momentum thickness (θ); (*c*) shape factor (H) and (*d*) longitudinal component of the pressure gradient ($\partial C_p/\partial x$).

Last, we have inspected the Reynolds stress tensor to obtain further insight into the turbulence activity within the boundary layer. The components of the Favre-averaged Reynolds stress tensor ($R_{ij} = \widetilde{u_i'' u_j''}$, where $(\cdot)''$ denotes the Favre fluctuating component) have been determined by locally decomposing the velocity field into tangential (t), normal (n) and spanwise (z) velocity components. Figure 17 shows the profiles of the tangential stress R_{tt} scaled in reference viscous units at five stations along the suction side. In the reference case, the stress is maximum upstream of the shock, ($x \approx 0.45$, second panel), the amplification being related to the formation of a mixing layer (Pirozzoli, Bernardini & Grasso 2010). Fang *et al.* (2020) have shown that in the decelerating region upstream of the foot of the shock, the adverse pressure gradient decelerates the boundary layer, thus increasing the production of turbulence kinetic energy via the longitudinal production term $-\widetilde{u_t'' u_t''}\partial\widetilde{u}/\partial\xi$. Hence, a positive feedback loop is established for the turbulent kinetic energy and, in particular, for $\widetilde{u_t'' u_t''}$, until the flow stops decelerating downstream of the shock. For simulation DR, the local maximum of R_{tt} takes place further downstream, at $x = 0.51$ (third panel). Upstream of the shock, case DR exhibits nearly halved fluctuations, whose peak is shifted away from the wall (from $\eta^+ \approx 10$ of the reference case to $\eta^+ \approx 30$).

https://doi.org/10.1017/jfm.2025.332 Published online by Cambridge University Press

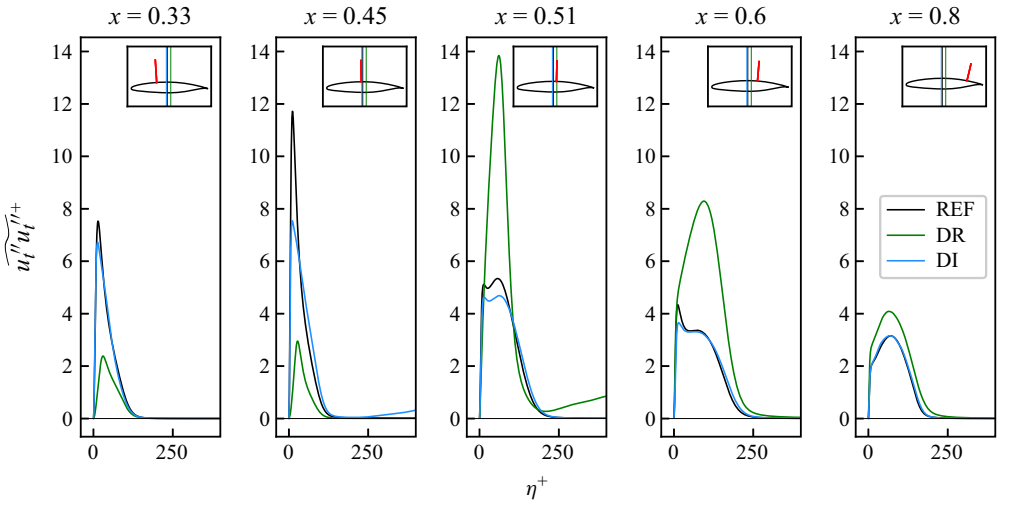


Figure 17. Profiles of tangential turbulent stress ($\widetilde{u_t''u_t''}$) along the wall-normal coordinate η, at five positions along the chord (whose streamwise coordinate is reported on top of each panel) for the REF, DR and DI flow cases. In the insets, the red lines denote the position along the chord and the orientation of the normal, while the vertical coloured lines show the positions of the shocks.

Flow case DI instead exhibits the opposite behaviour, with slight reduction of the peak, which also moves closer to the wall. Differences are striking at $x = 0.51$, which is upstream of the shock in case DR, but downstream of it in cases REF and DI. Looking at the two rightmost panels, the growth of the boundary layer is reflected in the larger wall distance of the peaks, which occurs at $\eta^+ \approx 90$. The monotonic decrease of $\widetilde{u_t''u_t''}$ confirms the gradual spreading of the mixing layer (Pirozzoli *et al.* 2010).

4.2. *Transient analysis*

To further elucidate the relationship between StTWs and flow reversal, we have analysed the transient following the sudden application of StTWs at $t = 0$. Specifically, flow samples separated in time by $\Delta t = 6.2 \times 10^{-3}$ have been collected over a time span of 16.6 convective time units after wall actuation is turned on. Figure 18 describes flow cases C10 (denoted as 'DR' so far) and C13; the former has a large reversed flow region, whereas in the latter, the region of reversal is significantly smaller. The left panels show the time history of spanwise-averaged quantities, additionally smoothed out by a running average over six time samples. The quantities are, from top to bottom, the local suction-side friction coefficient ($C_{f,l}$), defined here as the average over the streamwise interval $0.3 \leqslant x \leqslant 0.4$, the shock position x_s and the flow reversal length (L_r). The right panels plot two snapshots of the magnitude of the instantaneous field of the pressure gradient, $\|\nabla p\|$, plotted on an (x, y) plane at $t = 1.7$ and at $t = 16.6$. Movies for the evolution of the pressure gradient field over the transient are available online.

In both simulations, after enabling control at $t = 0$, the friction coefficient approaches its asymptotic value on a time scale that is short enough to be barely visible in the plots (top-left panels). A non-equilibrium state then ensues, as the reduced friction causes the shock to move downstream. This takes place on a much longer time scale, corresponding to approximately eight convective time units for flow case C10 and four time units for flow case C13. Flow reversal is present in flow case C10 since the earliest stages, intermittently at first, then growing as the shock moves downstream, and becoming nearly stationary

https://doi.org/10.1017/jfm.2025.332 Published online by Cambridge University Press

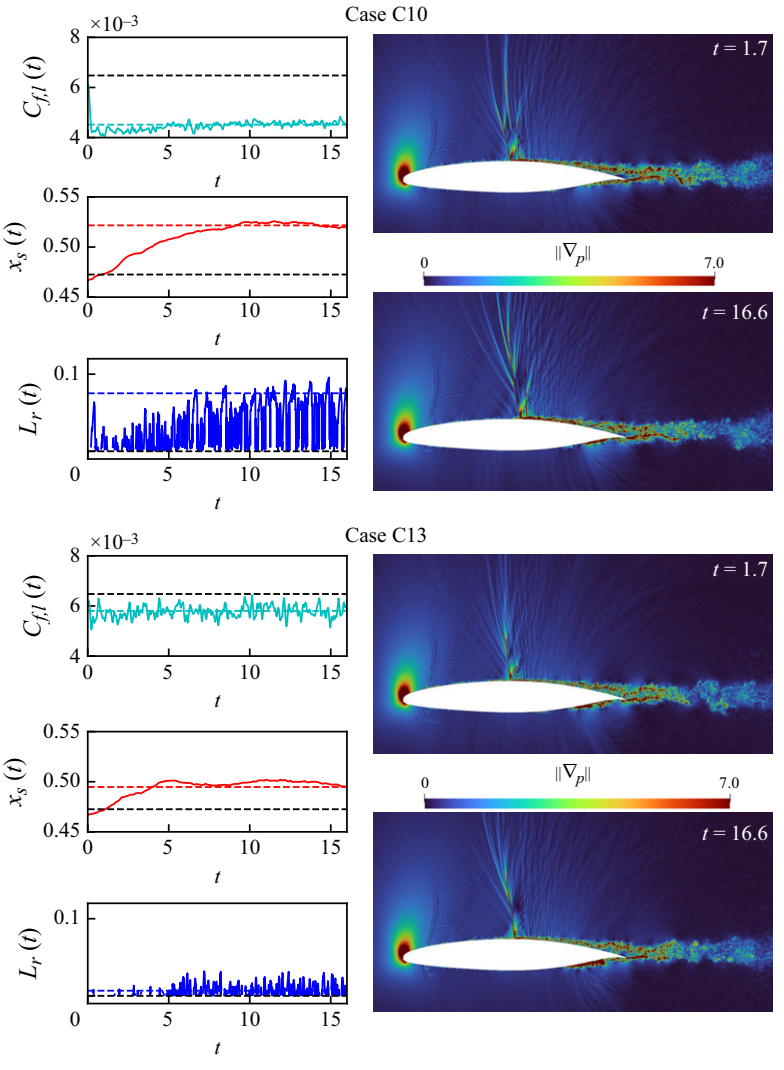


Figure 18. Transient of flow cases C10 (top) and C13 (bottom). On the left: time histories of the spanwise-averaged mean friction coefficient between $x = 0.3$ and $x = 0.4$ ($C_{f,l}(t)$, top), the shock position ($x_s(t)$, centre) and the length of the recirculation bubble ($L_r(t)$, bottom), after sudden activation of StTWs. The horizontal lines show the mean asymptotic value (coloured) and the mean value of the REF flow case (black). On the right: magnitude of the pressure gradient $\|\nabla p\|$ on an (x, y) plane, shortly after the control activation ($t = 1.7$) and at a later time ($t = 16.6$). Movies are available online.

for $t \gtrsim 8.2$. Flow case C13 initially features intermittent flow reversal, with relatively long time intervals with fully attached flow. Approximately five time units are needed for flow reversal to fully establish. Since the shock is located more upstream in C13, the intensity and extent of the adverse pressure gradient region is less, hence the final length of the reversed flow region is significantly smaller than for case C10.

Flow reversal past the shock is only an aspect of transonic shock wave / turbulent boundary layer interaction, which was analysed via DNS by Pirozzoli *et al.* (2010). Turbulent boundary layers hit by a shock tend to thicken upstream of the interaction owing to the strong pressure rise caused by the shock. This creates compression waves,

https://doi.org/10.1017/jfm.2025.332 Published online by Cambridge University Press

and, if the Mach number is large enough, induces a separation, ultimately resulting in a λ-shock configuration (Délery & Marvin 1986). The right panels of figure 18 display two different shock patterns. For flow case C10, at the short time $t = 1.7$, the lower part of the shock tilts, generating compression waves travelling downstream towards the trailing edge. During this motion, they encounter and merge with pressure waves from the wake at the trailing edge, resulting in a secondary, smaller shock, which stabilises quickly. Exchange of information via pressure waves takes place between the two shocks through both the supersonic and subsonic regions, until the system reaches a stable configuration around $t = 16$. It is worth noting that the final shock configuration resembles the typical topology of neither a weak shock/boundary layer interaction (i.e. with a single shock), nor a strong one (in which a λ-shock is formed). In flow case C13, we observe intensification of the shock with respect to its initial configuration, without the secondary shock. The time evolution from $t = 1.7$ onwards shows that pressure waves depart from the main shock and merge with those generated at the trailing edge, but they do vanish at $t \approx 8$.

Therefore, we conclude that StTWs affect first the turbulent boundary layer directly, on a very short time scale, by abating the friction coefficient locally. On a longer time scale, the reduced friction indirectly causes the shock to move towards the trailing edge; this induces global modifications of the wall pressure distribution and then of the entire boundary layer. Flow reversal, which seems to be more a consequence of the modification of the shock position rather than a direct effect of wall actuation, causes the development of a secondary supersonic region. Whenever the recirculating bubble is large enough, a second, weaker shock develops.

5. Concluding discussion

In this work, we have extended the study by Quadrio *et al.* (2022), describing the turbulent transonic flow around a three-dimensional wing slab where flow control made by StTWs of spanwise wall forcing is employed to improve the aerodynamic performance of the wing. Several direct numerical simulations have been carried out to explore the space of the control parameters, to compare the present results with the incompressible channel flow and to assess the effectiveness of StTWs in a typical aeronautical application.

Our findings confirm that StTWs, in addition to friction, also affect the other contributor to aerodynamic drag, i.e. pressure. The main consequence of StTWs is a varied position of the suction-side shock, which is shifted towards the trailing edge when the control parameters are properly selected to reduce friction. As a result, lift, drag and moment coefficients of the wing are all modified by the control. Interestingly, while lift increases significantly, drag is not much affected by StTWs, even though the forcing reduces friction locally as expected. This is due to an increase in pressure drag, resulting from an intensification of the shock. In fact, changes induced by StTWs to friction and pressure drag are comparable in magnitude. By studying the local contributions to the changes of the drag coefficient, we have been able to decouple the direct effects of the forcing from those deriving from the reduced angle of attack required to obtain the same lift. The aerodynamic efficiency of the aerofoil can rise up to 11 %, leading to a large reduction in the drag coefficient of the entire aircraft, together with a negligible actuation power. A qualitative estimate has placed the potential net savings for the entire aircraft at approximately 12 %. Such a large improvement of the aerodynamic performance implies that net savings could still be obtained with an actuator of efficiency as low as 0.045, thanks to the large benefits and the comparatively small amount of required energy, owing to the limited actuation area.

https://doi.org/10.1017/jfm.2025.332 Published online by Cambridge University Press

One question that we tackled, at least qualitatively, is whether our understanding of the optimal parameters for StTWs in the incompressible channel flow can be brought forward to the present, more complex application. Similarities with channel flows have been found in terms of friction drag reduction: by varying the control parameters, the reduction of the wall-shear stress evolves in a way that resembles that of the incompressible plane channel. However, a quantitative comparison with the channel flow is close to impossible, owing to additional curvature effects, the presence of pressure gradients and the unavoidable presence of spatial transients.

Through the analysis of the temporal transient after the imposition of wall forcing, we have described how the localised reduction of friction on the suction side of the wing alters the interaction between the shock wave and the turbulent boundary layer. While the response of wall friction to the wall-based actuation is quite fast, the evolution of the flow from the uncontrolled state to the quasi-stationary conditions with control is significantly longer. The initial local reduction in friction perturbs the state of equilibrium of the flow, eventually resulting in the downstream displacement of the shock. The process is relatively slow, taking place on a time scale of approximately eight convective time units. When the control parameters are optimally tuned, the downstream shift of the shock is significant and the shock becomes stronger: the turbulent boundary layer undergoes a stronger adverse pressure gradient and separates. In these cases, a small recirculation bubble, which may alter the topology of the shock system, appears beneath the shock. The length of the detached region, when present, is found to directly correlate with the values of friction drag reduction. Further works should explore the effects of changing Mach numbers on the aerodynamic performance of the controlled wing, to establish whether the improvements are only due to the shift (and the presence) of the shock wave.

The main limitation of this work consists in the low value of the Reynolds number, namely $Re_\infty = 3 \times 10^5$, which is not high enough to be representative of the typical flight conditions and leads to a subcritical turbulent boundary layer on a fraction of the wing. The numerical tripping required to guarantee a reasonable development of turbulence introduces an extra layer of arbitrariness. We believe that considering a flight Reynolds numbers of at least $Re_\infty = 10^6$ is required to provide the observations described in this work with a firmer physical ground. Nevertheless, drag reduction of the order of that observed in this study would represent a large improvement in terms of operational cost of transonic flight, and definitely motivates further research in the field of turbulent drag reduction in realistic flow configurations.

As a closing remark, we underline that the present conclusions should not be limited to spanwise forcing, as they naturally extend to any drag-reducing technology, including passive devices such as riblets, which are much closer than StTWs to industrial implementation. More than optimising the StTW control parameters for this specific wing, future work should properly formulate and solve an optimisation problem for the optimal layout and positioning for an actuator, or, equivalently, for a passive device for skin friction reduction. Since at least part of the cost for (active and passive) flow control directly relates to the covered surface area, whereas the benefit, as we have seen here, crucially depends on which area is selected, the designer will need to know how to deploy the control system optimally to achieve the best cost/benefit ratio.

Supplementary movies. Supplementary movies are available at https://doi.org/10.1017/jfm.2025.332.

Acknowledgements. All the simulations were performed on the Hawk Cluster in Stuttgart (Baden-Württemberg, Germany), within the project TuCoWi. The authors are grateful to Drs Alessandro Chiarini and Antonio Memmolo for their help in the initial stages of the work.

https://doi.org/10.1017/jfm.2025.332 Published online by Cambridge University Press

Funding. This research received no specific grant from any funding agency, commercial or not-for-profit sectors.

Declaration of interests. The authors report no conflict of interest.

Appendix A. How to define viscous scaling

As mentioned in § 3.2, a true comparison between the skin-friction drag-reducing properties of StTWs in the incompressible plane channel flow and the present transonic wing is unavoidably arbitrary to some extent. In this Appendix, we critically discuss our choice of extracting the friction velocity required to define viscous scaling at the specific position $x = 0.4$ and show the effect of alternative choices. In particular, we consider the positions $x = 0.3$, $x = 0.35$, $x = 0.4$, as well as the option of obtaining ΔC_f by averaging over the range $0.3 \leqslant x \leqslant 0.4$. All these positions are located at least 10 % downstream of the beginning of the control x_b and, at the same time, are sufficiently upstream of the shock position that the influence of the latter can be reasonably neglected.

Figure 19 shows the values of ΔC_f obtained from the present dataset, together with results interpolated from the incompressible channel flow data by Gatti & Quadrio (2016) for the same control input. From a global perspective, the results closest to the channel flow data are obtained in the central and right-most columns, corresponding to lines L2 and L3 of figure 3, respectively. In panels (a), (d), (g) and (j), corresponding to L1 of figure 3, the position of the peak of ΔC_f is shifted at lower frequencies for the wing, albeit the two curves are qualitatively similar. The obvious deduction is that the more downstream C_f is extracted, the more the quantity ΔC_f tends to the value of the incompressible channel flow, regardless of the control parameters. In particular, the location $x = 0.3$, whose results are depicted in panels (a), (b) and (c), is probably still too close to the beginning of the actuation, while the results closest to the channel flow data are those for $x = 0.4$ (panels g, h and i), i.e. where $\Delta C_f(x)$ is reaching a plateau.

By using actual viscous units computed with friction velocity at $x = 0.4$, figure 20 shows the wall-normal profiles of the mean streamwise velocity component, plotted according to the Trettel–Larsson scaling (Trettel & Larsson 2016) and coloured according to the skin-friction reduction rate ΔC_f. The profiles provide information on what would be the true Reynolds-independent measure of the skin-friction reduction in an indefinite plane channel, i.e. the wall-normal shift of the logarithmic layer of the streamwise velocity component Gatti & Quadrio (2016). It should be remarked, however, that the concept of logarithmic law should be used with caution here, as the flow has a rather low Re and is out of equilibrium. With this scaling, the viscous sublayer is obviously not affected by StTWs, whose effect is instead visible in the logarithmic region, where the curves are shifted towards higher values of u^* for a fixed η^* proportionally to the skin-friction reduction rate. The only curve below the reference one corresponds to case DI, in which C_f is indeed increased. The low Reynolds number of the simulations of this study, an issue mentioned in § 5, is reflected in figure 20 in the small range of wall-normal distances η^* in which the scaled streamwise velocity profile follows a linear law in logarithmic axis. This range, indeed, is similar to that observed in the study by Gatti & Quadrio (2016) in their figures 10(a) and 10(b), which show data at the lowest friction Reynolds number available ($Re_\tau = 200$).

Finally, figure 21 shows the wall-normal shift ΔB^* extracted at $\eta^* = 90$ for the set of simulations at constant forcing amplitude, computed on different stations of the suction

https://doi.org/10.1017/jfm.2025.332 Published online by Cambridge University Press

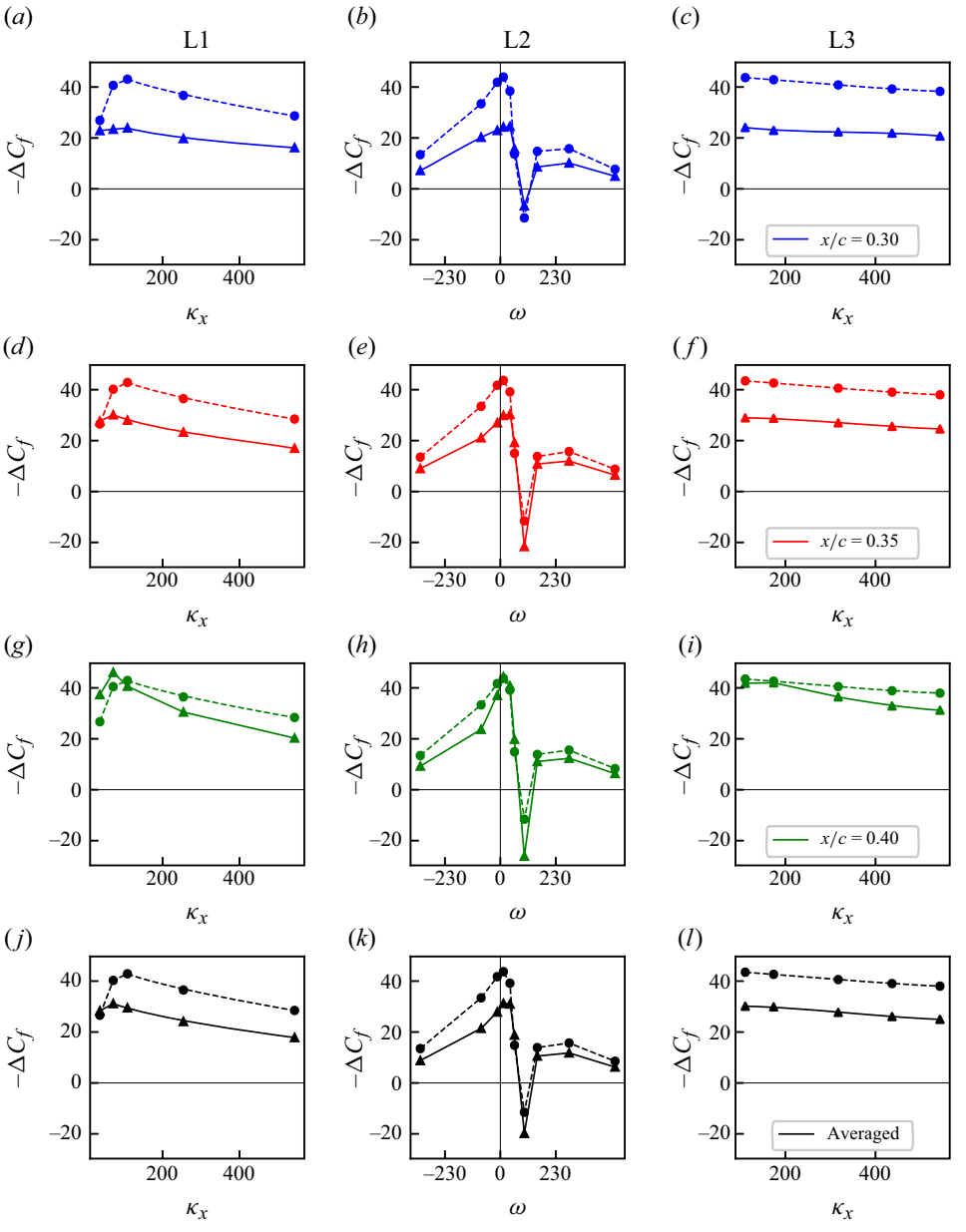


Figure 19. Dependence of ΔC_f upon the measurement position along the chord. Circles and dashed lines, channel flow data; triangles and solid lines, present data.

side of the wing. Additionally, the black curves show ΔB^* obtained considering the velocity profile averaged in the range $0.3 \leqslant x \leqslant 0.4$. The qualitative behaviour confirms the observations made in reference to figure 19 for the skin-friction coefficient, confirming that the two quantities are related, and that the conclusions by Gatti & Quadrio (2016) also apply to compressible boundary layers over mildly non-planar surfaces.

https://doi.org/10.1017/jfm.2025.332 Published online by Cambridge University Press

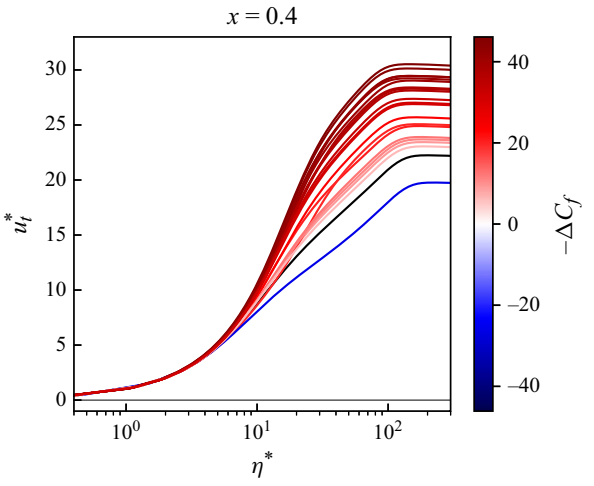


Figure 20. Wall-normal profile of the wall-parallel velocity component u_t, scaled in actual viscous units. The profiles for simulations C1–C20 (constant forcing amplitude A) are extracted at $x = 0.4$ and coloured according to the skin-friction reduction rate $-\Delta C_f$. The black line denotes the reference case REF.

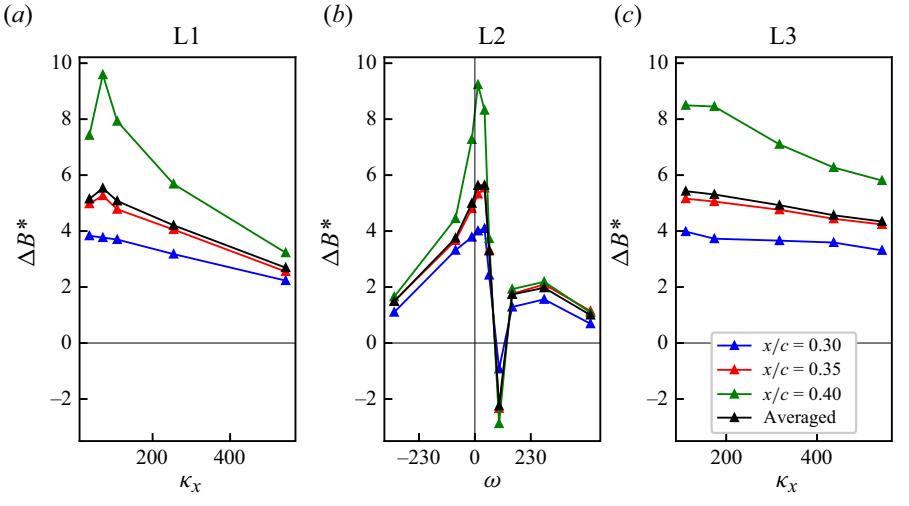


Figure 21. Wall-normal shift of the logarithmic layer of the streamwise velocity component for the simulations at constant A. The different curves denote different streamwise locations for extracting the data.

References

Abbas, A., de Vicente, J. & Valero, E. 2013 Aerodynamic technologies to improve aircraft performance. *Aerosp. Sc & Tech.* **28** (1), 100–132.

Auteri, F., Baron, A., Belan, M., Campanardi, G. & Quadrio, M. 2010 Experimental assessment of drag reduction by traveling waves in a turbulent pipe flow. *Phys. Fluids* **22** (11), 115103–115114.

Banchetti, J., Luchini, P. & Quadrio, M. 2020 Turbulent drag reduction over curved walls. *J. Fluid Mech.* **896**, 1–23.

Bird, J., Santer, M. & Morrison, J.F. 2018 Experimental control of turbulent boundary layers with in-plane travelling waves. *Flow Turbul. Combust.* **100** (4), 1015–1035.

Délery, J. & Marvin, J.G. 1986 Shock-Wave Boundary Layer Interactions. (ed. Reshotko, E.) AGARDograph 280. Advisory Group for Aerospace Research for Development, NATO, p. 224.

https://doi.org/10.1017/jfm.2025.332 Published online by Cambridge University Press

DOERFFER, P., FLASZYNSKI, P., DUSSAUGE, J.-P., BABINSKY, H., GROTHE, P. & PETERSEN, A. 2021 Transition Location Effect on Shock Wave Boundary Layer Interaction: Experimental and Numerical Findings from the TFAST Project, In *Notes on Numerical Fluid Mechanics and Multidisciplinary Design*. (ed. F. BILLARD), vol. 144. Springer International Publishing.

DUCROS, F., FERRAND, V., NICOUD, F., WEBER, C., DARRACQ, D., GACHERIEU, C. & POINSOT, T. 1999 Large-Eddy simulation of the shock/Turbulence interaction. *J. Comput. Phys.* **152** (2), 517–549.

FANG, J., ZHELTOVODOV, A., YAO, Y., MOULINEC, C. & EMERSON, D. 2020 On the turbulence amplification in shock-wave/turbulent boundary layer interaction. *J. Fluid Mech.* **897**, A32.

FROHNAPFEL, B., HASEGAWA, Y. & QUADRIO, M. 2012 Money versus time: evaluation of flow control in terms of energy consumption and convenience. *J. Fluid Mech.* **700**, 406–418.

FUMAROLA, I., SANTER, M. & MORRISON, J. 2024 Simultaneous measurements of surface spanwise waves and velocity in a turbulent boundary layer. *Flow Turbul. Combust.* **113** (1), 139–158.

GALLORINI, E. & QUADRIO, M. 2024 Spatial discretization effects in spanwise forcing for turbulent drag reduction. *J. Fluid Mech.* **982**, A11.

GATTERE, F., ZANOLINI, M., GATTI, D., BERNARDINI, M. & QUADRIO, M. 2024 Turbulent drag reduction with streamwise-travelling waves in the compressible regime. *J. Fluid Mech.* **987**, A30.

GATTI, D., GÜTTLER, A., FROHNAPFEL, B. & TROPEA, C. 2015 Experimental assessment of spanwise-oscillating dielectric electroactive surfaces for turbulent drag reduction in an air channel flow. *Exp. Fluids* **56** (5), 1–15.

GATTI, D. & QUADRIO, M. 2016 Reynolds-number dependence of turbulent skin-friction drag reduction induced by spanwise forcing. *J. Fluid Mech.* **802**, 553–558.

GRAVER, B., ZHANG, K. & RUTHERFORD, D. 2019 CO2 emissions from commercial aviation, 2018, Tech. Rep.International Council on Clean Transportion.

JAMESON, A., SCHMIDT, W. & TURKEL, E. 1981 Numerical solution of the Euler equations by finite volume methods using Runge Kutta time stepping schemes, In 14th Fluid and Plasma Dynamics Conference. American Institute of Aeronautics and Astronautics.

JUNG, W.J., MANGIAVACCHI, N. & AKHAVAN, R. 1992 Suppression of turbulence in wall-bounded flows by high-frequency spanwise oscillations. *Phys. Fluids A* **4** (8), 1605–1607.

KASAGI, N., HASEGAWA, Y. & FUKAGATA, K. 2009 Towards cost-effective control of wall turbulence for skin-friction drag reduction. In *Advances in Turbulence XII*, (ed. B. ECKHARDT), vol. **132**, pp. 189–200. Springer.

KNOOP, M.W., HARTOG, F.H., SCHRIJER, F.F.J., VAN CAMPENHOUT, O.W.G., VAN NESSELROOIJ, M. & VAN OUDHEUSDEN, B.W. 2024 Experimental assessment of square-wave spatial spanwise forcing of a turbulent boundary layer. *Exp. Fluids* **65** (5), 65.

LAFLIN, K.R., KLAUSMEYER, S.M., ZICKUHR, T., VASSBERG, J.C., WAHLS, R.A., MORRISON, J.H., BRODERSEN, O.P., RAKOWITZ, M.E., TINOCO, E.N. & GODARD, J.-L. 2005 Data summary from second AIAA computational fluid dynamics drag prediction workshop. *J. Aircraft* **42** (5), 1165–1178.

LIU, X.D., OSHER, S. & CHAN, T. 1994 Weighted essentially non-oscillatory schemes. *J. Comp. Phys.* **115**, 200–212.

MARUSIC, I., CHANDRAN, D., ROUHI, A., FU, M.K., WINE, D., HOLLOWAY, B., CHUNG, D. & SMITS, A.J. 2021 An energy-efficient pathway to turbulent drag reduction. *Nat. Commun.* **12** (1), 5805.

MELE, B., TOGNACCINI, R. & CATALANO, P. 2016 Performance assessment of a transonic wing-body configuration with riblets installed. *J. Aircraft* **53** (1), 129–140.

MEMMOLO, A., BERNARDINI, M. & PIROZZOLI, S. 2018 Scrutiny of buffet mechanisms in transonic flow. *Intl J. Numer. Meth. Fluids* **28** (5), 1031–1046.

PIROZZOLI, S. 2011 Numerical methods for high-speed flows. *Annu. Rev. Fluid Mech.* **43** (1), 163–194.

PIROZZOLI, S., BERNARDINI, M. & GRASSO, F. 2010 Direct numerical simulation of transonic shock/boundary layer interaction under conditions of incipient separation. *J. Fluid Mech.* **657**, 361–393.

PLACEK, R. & RUCHALA, P. 2018 The flow separation development analysis in subsonic and transonic flow regime of the laminar airfoil. *Transp. Res. Proc.* **29**, 323–329.

QUADRIO, M., CHIARINI, A., BANCHETTI, J., GATTI, D., MEMMOLO, A. & PIROZZOLI, S. 2022 Drag reduction on a transonic airfoil. *J. Fluid. Mech.* **942**, 1–10.

QUADRIO, M. & RICCO, P. 2004 Critical assessment of turbulent drag reduction through spanwise wall oscillations. *J. Fluid Mech.* **521**, 251–271.

QUADRIO, M. & RICCO, P. 2011 The laminar generalized Stokes layer and turbulent drag reduction. *J. Fluid Mech.* **667**, 135–157.

QUADRIO, M., RICCO, P. & VIOTTI, C. 2009 Streamwise-traveling waves of spanwise wall velocity for turbulent drag reduction. *J. Fluid Mech.* **627**, 161–178.

https://doi.org/10.1017/jfm.2025.332 Published online by Cambridge University Press

RUSSO, S. & LUCHINI, P. 2017 A fast algorithm for the estimation of statistical error in DNS (or experimental) time averages. *J. Comput. Phys.* **347**, 328–340.

SCHLATTER, P. & ÖRLÜ, R. 2012 Turbulent boundary layers at moderate Reynolds numbers: inflow length and tripping effects. *J. Fluid Mech.* **710**, 5–34.

SKOTE, M. 2012 Temporal and spatial transients in turbulent boundary layer flow over an oscillating wall. *Intl J. Heat Fluid Flow* **38**, 1–12.

SMITS, A.J. & DUSSAUGE, J.P. 2006 *Turbulent Shear Layers in Supersonic Flow*. Springer.

SPALART, P. & ALLMARAS, S. 1992 A one-equation turbulence model for aerodynamic flows, In 30th Aerospace Sciences Meeting and Exhibit. American Institute of Aeronautics and Astronautics.

SZUBERT, D., ASPROULIAS, I., GROSSI, F., DUVIGNEAU, R., HOARAU, Y. & BRAZA, M. 2016 Numerical study of the turbulent transonic interaction and transition location effect involving optimisation around a supercritical aerofoil. *Eur. J. Mech. (B/ Fluids)* **55**, 380–393.

TRETTEL, A. & LARSSON, J. 2016 Mean velocity scaling for compressible wall turbulence with heat transfer. *Phys. Fluids* **28** (2), 026102.

VENKATAKRISHNAN, V. 1995 Convergence to steady state solutions of the Euler equations on unstructured grids with limiters. *J. Comput. Phys.* **118** (1), 120–130.

XU, D., RICCO, P. & DUAN, L. 2023 Decomposition of the skin-friction coefficient of compressible boundary layers. *Phys. Fluids* **35** (3), 035107.

YAO, J. & HUSSAIN, F. 2019 Supersonic turbulent boundary layer drag control using spanwise wall oscillation. *J . Fluid Mech.* **880**, 388–429.

YUDHISTIRA, I. & SKOTE, M. 2011 Direct numerical simulation of a turbulent boundary layer over an oscillating wall. *J. Turbul.* **12** (9), 1–17.

ZAUNER, M., DE TULLIO, N. & SANDHAM, N.D. 2019 Direct numerical simulations of transonic flow around an airfoil at moderate Reynolds numbers. *AIAA J.* **57** (2), 597–607.

https://doi.org/10.1017/jfm.2025.332 Published online by Cambridge University Press